Harmonic Generation and Long-Range Optical Binding of Aerosols

by

Jeremy John Moore

A dissertation submitted in partial fulfillment
of the requirements for the degree of
Doctor of Philosophy
(Electrical Engineering)
in The University of Michigan
2014

Doctoral Committee:

Professor Tal Carmon, Co-Chair
Professor Stephen Rand, Co-Chair
Professor L. Jay Guo
Professor Jens-Christian Meiners

For Melissa.

ACKNOWLEDGEMENTS

I would like to acknowledge the help and guidance of all the people who contributed to this work. My advisor, Professor Tal Carmon, of course deserves special mention. Without his creative vision and support, I would never have been able to complete my doctoral research work. I would also like to acknowledge the contribution of the other members of my research group, Mark Dong, Kyu Hyun Kim, Dr. Hengky Chandrahalim, Professor Gaurav Bahl, and especially Dr. Matthew Tomes. Their help and collaboration have been invaluable.

Thanks also to my committee members and the many students, professors, and staff with whom I have worked for the last six years at the University of Michigan. In particular, I would like to thank Dr. Chris Berry and Dr. Leopoldo Martin for their insight and collaboration on many different experiments.

Much of the experimental work in this dissertation owes its completion to advice and assitance from Prof. Mani Hossein-Zadeh, Dr. Harald Schwefel, and Dr. Matt Eichenfield.

Last, I would like to thank my family. My sister Rachel, my brother Brandon, my parents, my grandparents, my partner Melissa, and the rest of my family have done everything possible to help me see this work through. Thank you all so much for your love and support.

TABLE OF CONTENTS

LIST OF FIGURES

Figure

LIST OF TABLES

Table

LIST OF APPENDICES

Appendix

ABSTRACT

Harmonic Generation and Long-Range Optical Binding of Aerosols

by

Jeremy Moore

Co-chairs: Tal Carmon and Stephen Rand

This dissertation presents the results of two major optical experiments. The first is the generation of continuous-wave ultraviolet light from an infrared pump laser by fourth harmonic generation in a lithium niobate whispering gallery resonator. The UV fourth harmonic (as well as the near-infrared second and visible third harmonics) is observed at input powers as low as 200mW, and is detected on a spectrum analyzer and photographed directly after outcoupling from a diamond prism. The emitted light is tunable over a pump range of 1535 to 1545nm, due to quasi-phase matching with a variable crystal poling period and high order modes in the resonator. This work extends previously observed second harmonic generation in similar devices to wavelengths near 385nm, demonstrating a compact, coherent UV source, and providing a first step toward high harmonic generation at CW operation.

The second experiment is the observation of long-range optical binding of aerosols in a vertical Gaussian beam optical trap. We demonstrate optical binding of 7-25μm diameter objects in a weakly focused Gaussian beam trap. In contrast to prior work in viscous liquids, the observed optical interactions take place in air, and without the use of interference techniques to create an optical potential landscape.

CHAPTER I

Introduction

This work describes experimental observations related to the interaction of light with matter and structure. Two major research topics are described in the following chapters. The first is the experimental demonstration of cascaded harmonic generation in a whispering gallery resonator, producing continuous wave ultraviolet light from a near infrared pump laser. The second discusses the observation of long-range interaction of opticall trapped dielectric objects. This so-called optical binding is investigated, and the static and dynamic behavior of the trapped objects is examined. The layout of the chapters is is as follows.

1.0.1 Chapter Overview

Chapter 2 provides an introduction to optical cavities, also known as resonators. Important parameters of optical cavities are discussed. Whispering gallery resonators are introduced, and important characteristics and applications are described.

Chapter 3 provides an introduction to nonlinear optics. Background is given on the nonlinear electric polarization of materials, and relevant nonlinear interactions and concepts are introduced. These include cascaded harmonic generation and stimulated Raman scattering.

Chapter 4 describes the demonstration of continuous-wave fourth harmonic gen-

eration in a lithium niobate whispering gallery resonator. Ultraviolet light is shown to be generated from a near infrared pump laser via cascaded $\chi^{(2)}$ processes. Additionally, multi-photon Raman scattering processes are investigated in the same resonator. The design and fabrication of the device are described, and the experimental procedure and results are discussed. The major findings in this chapter appear in (1) and (2).

Chapter 5 gives an introduction to the second part of this dissertation, optical binding of aeorsols. Background information on optical trapping and optical binding are presented.

Chapter 6 discusses the demonstration of long-range, underdamped otpical binding of aerosols. The experimentally observed behavior and interaction of objects confined to the same optical potential well trap are discussed. The initial work in this chapter was presented in (3).

Chapter 7 concludes the thesis and summarizes the major results.

CHAPTER II

Optical Resonators

This chapter provides an introduction to optical cavities, also known as resonators. Important parameters and background on resonators in general are reviewed in the first section. The second section introduces whispering gallery resonators and discusses their design, characteristics, and applications.

2.1 Optical Resonators

Optical resonators are devices or systems which allow light to circulate in a closed path. One of the most important classes of optical components, resonators have an enormous array of applications in many fields, including

- Laser feedback
- Optical filtering
- Interferometry
- Optical frequency standards
- Intensity enhancement

The simplest incarnation of an optical resonator is the Farbry-Perot cavity or etalon, which consists of two parallel reflecting surfaces (Figure 2.1). Fabry-Perot

resonators can be as simple as a single piece of dieletric material with two polished surfaces, or can be extremely complex and sophisticated systems composed of precisely aligned components.

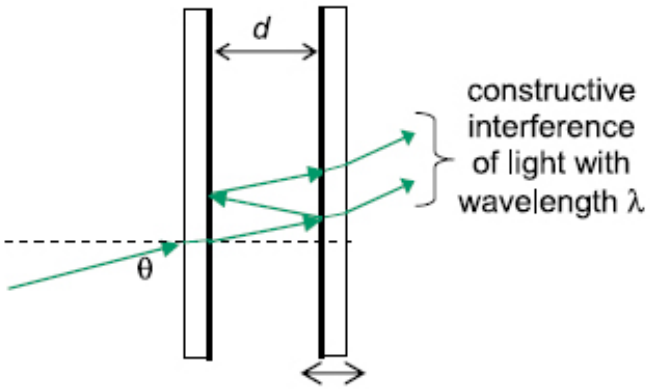

Figure 2.1: Schematic representation of a simple Fabry-Perot optical cavity. Two parallel mirrors reflect light in a closed path

Inside a Fabry-Perot cavity, light reflects from the parallel surfaces and travels back and forth between the mirrors. Constructive interference occurs for wavelengths of light that satisfy the condition

$$m\frac{\lambda}{n} = 2L \tag{2.1}$$

where L is the separation between the mirrors, m is an integer, n is the index of refraction, and λ is the free-space wavelength of the light. For these wavelengths, light making one round trip is in phase with light entering the cavity, and so incident and reflected electric field will add constructively. This allows electromagnetic energy to build up inside the resonator.

The quality factor, Q, quantifies the ability of a resonator to store energy. It is defined is as the ratio of the energy stored in the resonator to the energy lost in one optical cycle.

$$Q = 2\pi \frac{\text{Total Energy Stored}}{\text{Energy Lost Per Optical Cycle}}, \tag{2.2}$$

Alternately, the quality factor can be defined in terms of the bandwidth of the resonances. In this case, Q is defined as the ratio of the resonance frequency to the full width and half-maximum of the resonance:

$$Q = \frac{f_0}{\delta f}, \tag{2.3}$$

The energy storage capacity of the a resonator with a lossless medium is determined by the mirror reflectivity. The resonators finesse $\mathcal{F}$ is determined by these losses. For a symmetric Fabry-Perot, finesse is defined as

$$\mathcal{F} = \pi\sqrt{R}/(1-R), \tag{2.4}$$

where R is the power reflectance of the mirrors. The resonator finesse can be understood as the number of round trips that a photon will make before being absorbed, or, equivalently, the amplification of the input power inside the resonator. $\mathcal{F}$ and Q are related by

$$\mathcal{F} = \frac{Q\lambda}{2nL} \tag{2.5}$$

For a given cavity of a fixed length, there will be an infinite number of longitudinal modes which satisfy 2.1. The frequency separation between resonant modes, the free spectral range (FSR) of the cavity, is given by

$$FSR = \frac{c}{2nL}, \tag{2.6}$$

where c is the speed of light.

The last important parameter of optical cavities discussed in this section is mode volume V, defined as

$$V = \frac{\int_V |E|^2}{max|E^2|} \tag{2.7}$$

which describes the ability of a cavity to spatially confine light. Smaller mode volume in a resonator corresponds to greater intensity enhancement

In addition to Fabry-Perot cavities, there a large variety of configurations possible for optical resonators. Additional examples of optical resonators include triangular or bow-tie configurations using mirrors, distributed Bragg cavites, fiber based resonators, and photonic crystal microcavities.

2.2 Whispering Gallery Resonators

2.2.1 History

Whispering gallery resonators are a special class of circular optical cavities, in which light propagates azimuthally around the circumference of the resonator. Similar to the case of the Fabry-Perot, resonant wavelengths are determined by the condition that constructive inteference occurs after one round trip.

Optical whispering gallery resonators take their name from their acoustic analog, first described by Lord Rayleigh in 1910. He investigated the behavior of sound waves in St. Paul's Cathedral, London (Figure 2.2 (4)), where "sonorous vibrations have a tendency to cling to concave surfaces." (5). A person can whisper against the domed wall of the cathedral and hear the sound of their own voice that has propagated around the room.

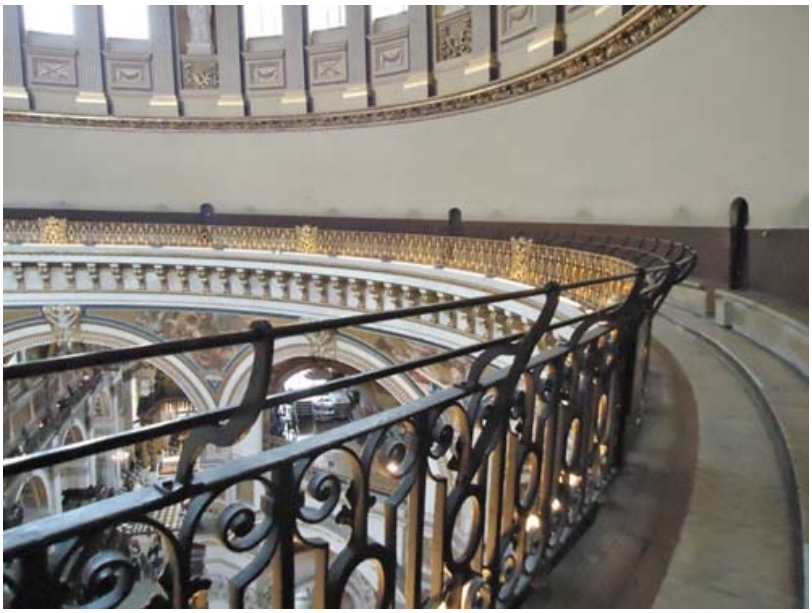

Figure 2.2: St. Paul's Cathedral, London, where Lord Rayleigh first described acoustic whispering gallery resonators

Around the same time, Debye formulated expressions for the resonant frequencies of spherical objects made of metal and dielectrics (which include whispering gallery modes) (6) and Mie investigated the scattering of electromagnetic radiation by spheres (7). These studies represented the earliest work on electromagnetic whispering gallery resonators.

2.2.2 Whispering Gallery Resonator Properties and Applications

Practical whispering gallery resonators come in many forms, including

- Aerosols (8)
- On-chip silica toroids (9)
- Fiber tip silica microspheres (10)
- Nanoimprinted polymer rings (11; 12)
- Polished crystalline disks (1)
- Liquid droplets (13)
- Hollow glass structures (14; 15)

Light is confined inside the resonator via total internal reflection, and ultrasmooth surfaces can be achieved either by surface tension (as in the case of melting and reflowing a fused silica resonator) or by mechanical polishing. In both cases, very low loss cavities have been achieved, which has allowed the demonstration of extremely high quality factors. Resonators have been fabricated with Q values up to 10^{11}, and finesses as large as 10^7 in CaF_2 (16).

In addition to high values of Q, small mode volumes have been demonstrated in a variety of whispering gallery resonators. Whispering gallery cavities have also been fabricated from a wide range of liquid and solid materials, enabling the demonstration of many novel effects. Figure 2.3 shows several types of whispering gallery resonators (17; 9; 14; 11; 13).

The large enhancement light intensity via multiple recirculations, and the large light-matter interaction distances (18; 19; 20), have enabled the demonstration of a wide variety of nonlinear phoenomena with low power, continuous-in-time excitation. Some of these include optomechanical vibrations (17; 21; 22; 23; 24), parametric

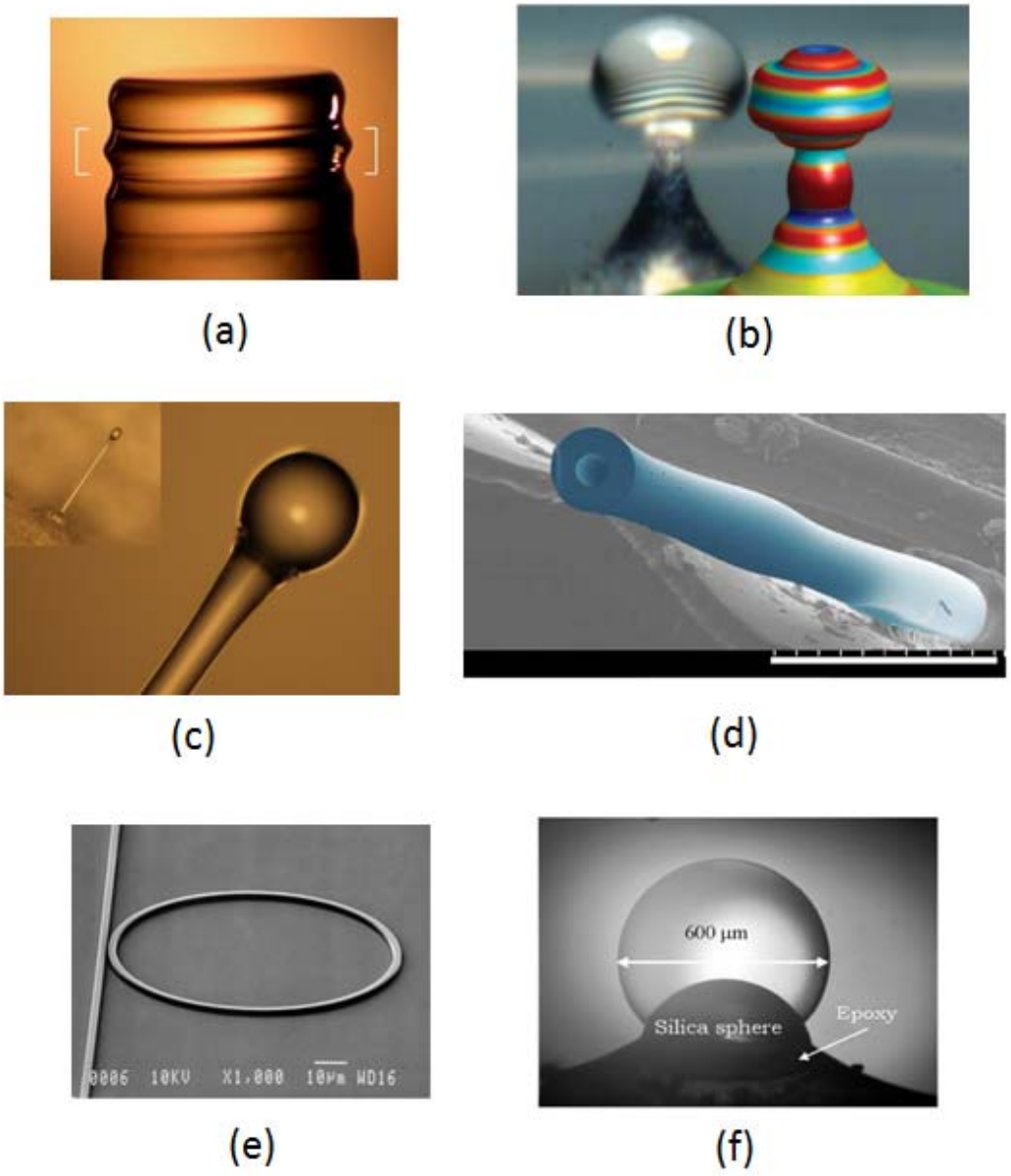

Figure 2.3: Examples of whispering gallery resonators. (a) CaF_2 (17) (b) on chip fused silica microtoroid (9) (c) fiber tip slica microsphere (d) microfluidic silica "bottle" (14) (e) polymer microring (11) and (f) liquid microsphere (13)

oscillations (25; 16; 26; 27), Raman-lasers (28; 29; 30), Erbium-lasers (31), Brillouin-lasers (17; 21; 22; 23), and continuous-wave second- and third-harmonic generation (32; 33; 34; 35; 36; 37; 27). Nonlinear optics, including several of the processes observed in whispering gallery resonators, is covered in following chapters.

2.2.3 Resonance Frequency Calculations

The condition for frequency resonance in whispering gallery geomteries is more complex than in the case of Fabry-Perot cavites, and many geometries require numerical simulation for calculating resonant modes, including finite element (FEM) (1; 38) and finite-difference time-domain (FDTD) techniques. Finite element mode calculations will be discussed in greater detail in following chapters.

For the simple case of a dielectric sphere, however, analytical solutions exist (39). Transverse electric (TE) modes are defined as modes with no radial component of the electric field (i.e. modes with polarization parallel to the axis of rotation of the resonator). Transverse magnetic (TM) modes are defined as those with no radial component of the magnetic field (i.e. modes with electric field polarization in parallel to the raidal direction). For TE modes, the resonant wavelength is given by

$$\frac{\Psi_n'(mx)}{\Psi_n(mx)} - m\frac{\zeta_n'(x)}{\zeta_n(x)} = 0 \tag{2.8}$$

where Ψ_n and ζ_n are Bessel and Hankel functions, respectively, m is the refractive index, n is the azimuthal mode order, and $(')$ denotes derivation with respect to the dimensionless size parameter

$$x = \frac{2\pi a}{\lambda} \tag{2.9}$$

where a is the radius of the sphere.

For TM modes, the corresponding expression is

$$m\frac{\Psi_n'(mx)}{\Psi_n(mx)} - \frac{\zeta_n'(x)}{\zeta_n(x)} = 0 \tag{2.10}$$

In cases where the azimuthal mode order is large (i.e. $a >> \lambda$), these solutions can be approximated by the expressions (19)

$$k_{n,q} \simeq \frac{1}{a\sqrt{\epsilon_0}}\left[n + \alpha_q\left(\frac{n}{2}\right)^{1/3} - \sqrt{\frac{\epsilon_0}{\epsilon_0 - 1}} + \frac{3\alpha_q^2}{20}\left(\frac{2}{n}\right)^{1/3} + O(n^{-2/3})\right] \tag{2.11}$$

where k is the wave vector, a is the sphere radius, n is the azimuthal mode order, and α_q is the q^{th} root of the Airy function. The expression for TM modes is similar:

$$k_{n,q} \simeq \frac{1}{a\sqrt{\epsilon_0}}\left[n + \alpha_q\left(\frac{n}{2}\right)^{1/3} - \sqrt{\frac{1}{\epsilon_0(\epsilon_0 - 1)}} + \frac{3\alpha_q^2}{20}\left(\frac{2}{n}\right)^{1/3} + O(n^{-2/3})\right] \tag{2.12}$$

An example of mode calculation for a 100μm silica microsphere is given in the appendix.

2.2.4 Coupling

Several methods exist for coupling light into whispering gallery resonators. Early experiments with aerosols relied on the coupling of a free space beam to whispering gallery modes of microscopic dielectric paricles (39). However, the efficiency of coupling to high Q whispering gallery modes from a free-space beam becomes extremely small as the resonator is increased in size above a few wavelengths (19).

Most methods of transfering energy to whispering gallery modes rely on the use of

evanscent near field coupling. In order to couple efficiently, the modes in the coupler must be spatially overlapped and phase matched. Common couplers for whispering gallery resonators include

- Dielectric waveguides
- Prisms
- Angle polished optical fibers
- Tapered optical fibers

The most efficient coupling is typically achieved with tapered fiber coupling, shown in Figure 2.4. A bare single mode fiber is heated (typically with a hydrogen flame or ceramic heater) and mechanically stretched, reducing the diameter in the coupling region. Greater than 99% coupling efficiency is possible, as has been shown in fused silica whispering gallery resonators.

Although tapered fibers are efficient couplers, they are also mechanically fragile. Typical diameters are on the order of $1\mu m$, and so maintaining a fiber coupler intact for long periods of time is challenging. Also, nano-scale positioning of the fiber is required for critical coupling. Finally, it can be difficult to match the mode and resonator indices in the case of high refractive index resonators.

Prism couplers, although less efficient than tapered fibers, address some of these limitations. Coupling to whispering gallery mode is achieved in a prism or angle polished fiber by means of frustrated total internal reflection. A laser is guided through the prism and the angle of incidence is chosen such that the beam undergoes total internal reflection from one face of the prism. The prism index and angle are chosen to match the propagation constants of the beam in the prism and the resonator mode. In the case of the angle polished fiber, and optical fiber is cleaved at an angle and the cleaved surface is polished to create an effective prism. Prism coupling is discussed in more detail in later chapters.

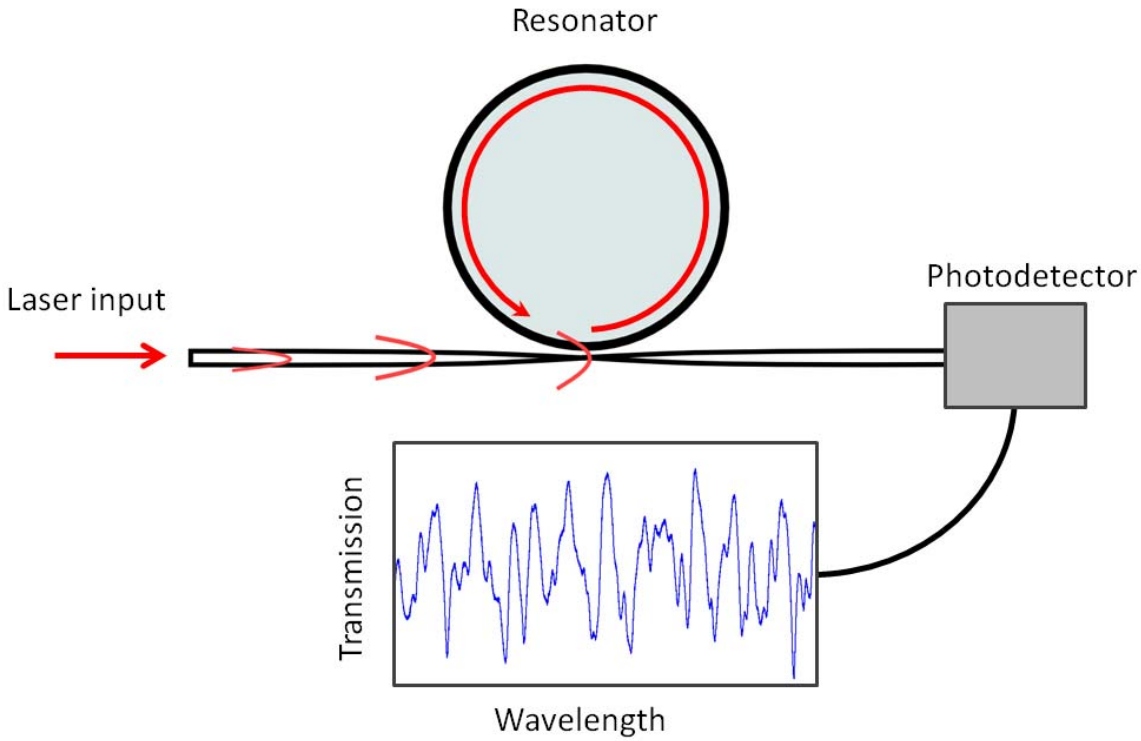

Figure 2.4: Tapered fiber coupler setup. An optical fiber is stretched over a heat source, thinning it adiabatically. The evanescent tail of the fiber mode couples to high Q whispering gallery modes, resulting in a decrease in transmission at resonant frequencies

2.3 Conclusion

Whispering gallery resonators are an important class of optical cavities with many desirable parameters. The high quality factors, small mode volumes, and simple structure of these devices has enabled the demonstration of a large number of nonlinear phenomena with low power, continuous-in-time excitation. The application of whispering gallery resonators to nonlinear optics, in particular cascaded harmonic generation, is described in the following chapters.

CHAPTER III

Nonlinear Optics

This chapter provides an introduction to topics in nonlinear optics related to the experimental work presented in later chapters. Background is given on harmonic generation, sum-frequency generation, and Raman scattering.

3.1 Introduction

Nonlinear optics is a branch of optics concerning optical phenomena which occur when intense light alters the properties of a material system. More specifically, this field focuses on the behavior of light in situations where the nonlinear polarization P of a medium depends nonlinearly on the electric field strength E of the light. For example, in the second harmonic generation, the material response depends quadratically on the field strenght, and so the intensity of output (which will have twice the input frequency) will depend quadratically on the intensity of the pump.

The intensities required to observe nonlinear effects are typically produced with laser light. Because of this, the study of nonlinear optics began shortly after the demonstration of the first laser in 1960 (40). The first experimental discovery in nonlinear optics occurred at the University of Michigan in 1961, with second harmonic generation of a ruby laser in quartz (41).

Nonlinear effects are often used to convert light produced by available sources to

frequencies which are not as readily accessible. Harmonic generation, sum-frequency and difference-frequency generation, four-wave mixing, optical parametric oscillation, and stimulated Raman scattering are some of the most commonly encountered nonlinear processes.

3.2 Nonlinear Polarization

Light propagating in a dielectric medium induces a dipole moment, or electrical polarization, in the material. This polarization propagates along with the optical wave. The expression for the nonlinear polarization of a material is

$$P(t) = \chi^{(1)}E(t) + \chi^{(2)}E^2(t) + \chi^{(3)}E^3(t) + \chi^{(4)}E^4(t)... \tag{3.1}$$

where $\chi^{(1)}$ is the linear susceptibility, $\chi^{(2)}$, $\chi^{(3)}$, $\chi^{(4)}$, etc. are the second order, third order, fourth order, etc. nonlinear susceptibilities, and E is the time dependent electric field amplitude. At low optical intensities, Eq. 3.1 reduces to the familiar linear case

$$P(t) = \chi^{(1)}E(t) \tag{3.2}$$

With high intensity, a nonlinear medium (i.e. a material posessing appreciable nonlinear susceptibility) will allow a pump laser to generate a nonlinear polarization wave, which will in turn radiate light at different frequencies, as described in the next section.

3.3 Nonlinear Interactions

3.3.1 Harmonic Generation

For a lossless medium, a pump laser with electric field given by

$$E(t) = Ee^{-i\omega t} + (\text{complex conjugate (c.c.)}) \tag{3.3}$$

will generated (ignoring higher order terms) a second order nonlinear polarization

$$P(t)^2 = \chi^{(2)}E(t)^2 \tag{3.4}$$

which can also be written as

$$P^{(2)}(t) = 2\chi^{(2)}EE^* + \chi^{(2)}E^2e^{-i2\omega t} + \text{c.c.} \tag{3.5}$$

The first term on the right side of Eq. 3.5 has no frequency dependence, and represents the introduction of a static electric field created within the medium. This process is known as optical rectification, and has been used to efficiently generated terahertz radiation from near infrared lasers (42). The second term on the right hand side of the equation has a frequency term at 2ω, which can lead to the generation of an optical signal at twice the pump frequency. This process is known as second harmonic generation or optical parametric amplification. An energy level description of the second harmonic generation process is shown in Figure 3.1. In the figure, two pump photons with frequency ω are destroyed, and a second harmonic photon with frequency 2ω is created. The solid line represents the atomic ground state, while

the dashed lines are virtual energy levels. These virtual states represent combined energies of the atomic eigenstates and photons, rather than eigenstates of the free atom.

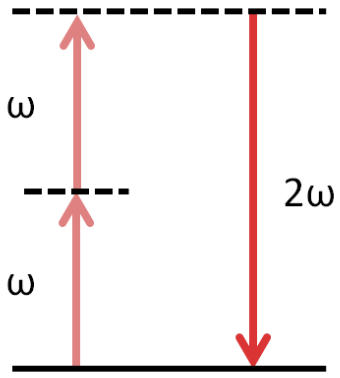

Figure 3.1: Second harmonic generation energy level description. Two photons of pump frequency ω_1 are absorbed, and a second harmonic photon of frequency ω_2 is emitted. The dashed lines represent virtual energy levels

An experimental configuration for second harmonic generation in a nonlinear crystal is shown in Figure 3.2.

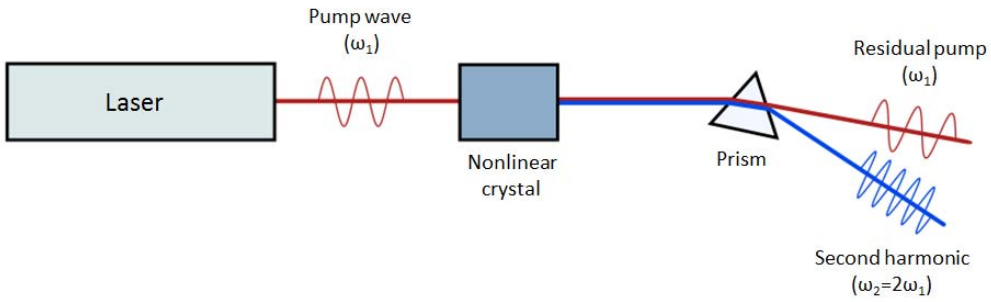

Figure 3.2: Second harmonic generation in a nonlinear crystal. The second harmonic frequency at $2\omega_1$ is separated from the pump with a prism.

Similarly, the third and fourth order nonlinear susceptibility leads to a polarization term with $e^{-i3\omega t}$ and $e^{-i4\omega t}$ dependence, which produce third and fourth harmonic generation, respectively.

The result of harmonic generation is the conversion of a pump laser to shorter wavelengths λ/n, where n is an integer. This technique can be efficient, and is widely used to create laser sources at unavailable wavelengths, including the ultraviolet region of the electromagnetic spectrum. With extremely intense laser pulses, very high order harmonics can be generated, reaching into the deep UV and x-rays (43).

3.3.2 Sum-Frequency Generation

In addition to permitting the generation of harmonics, the nonlinear response of materials enables the mixing of optical frequencies, including sum- and difference-frequency generation. For two pump waves given by

$$E(t) = E_1 e^{-i\omega_1 t} + E_2 e^{-i\omega_2 t} + \text{ (c.c.)} \tag{3.6}$$

is again

$$P(t)^2 = \chi^{(2)} E(t)^2 \tag{3.7}$$

With two pump fequencies, Eq. 3.8, produces and optical rectification term

$$P^{(2)}(t) = 2\chi^{(2)}(E_1 E_1^* + E_2 E_2^*) + \text{c.c.} \tag{3.8}$$

as well as two second harmonic terms (one for each pump)

$$\chi^{(2)} E_1^2 e^{-i2\omega_1 t} \tag{3.9}$$

$$\chi^{(2)} E_2^2 e^{-i2\omega_2 t} \tag{3.10}$$

Additionally, there are now additional terms, including

$$2\chi^{(2)} E_1 E_2 e^{-i(\omega_1+\omega_2)t} \tag{3.11}$$

$$2\chi^{(2)} E_1 E_2 e^{-i(\omega_1-\omega_2)t} \tag{3.12}$$

The frequency terms at $\omega_1 + \omega_2$ and $\omega_1 - \omega_2$ represent sum- and difference- frequency generation, respectively. The radiated light from these polarization terms will produce light with a frequency that is either the sum or the difference of the pump frequencies. An energy diagram repesentation of the sum- and difference-frequency generation processes is shown in Fig. 3.3.

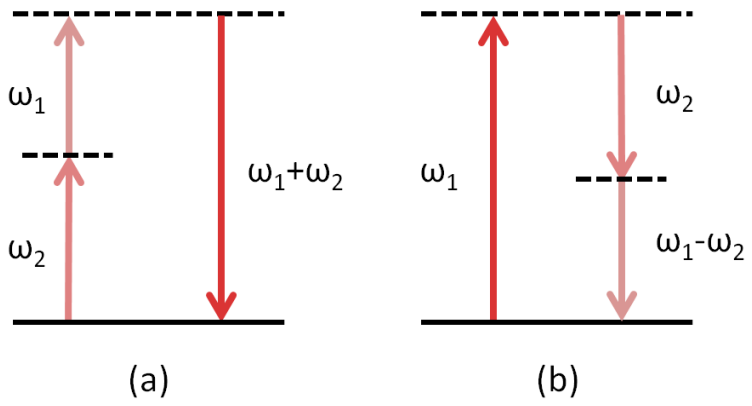

Figure 3.3: Energy level diagram for (a) sum and (b) difference frequency generation. In sum-frequency generation, two photons ω_1 and ω_2 are added to produce a third photon. In difference-frequency generation, ω_2 is subtracted from ω_1

Sum-frequency generation, like harmonic generation, can be used to convert the pump photons to higher energies. In the case of closely spaced input frequenices, difference-frequency generation can be used to produce far infrared and terahertz radiation.

3.3.3 Cascaded Harmonic Generation

Cascaded harmonic generation is a nonlinear phenomena which can produce both even and odd ordered harmonics λ/n by means of second order nonlinearity. Figure 3.4 shows an example of this process, which is a combination of harmonic generation and sum-frequency generation. In this case, the generated second harmonic is added to the pump, producing a third harmonic. This third harmonic is then added to the pump again, producing a fourth harmonic. The experimental observation of this process, producing continuous wave ultraviolet light from a $1.5\mu m$ pump laser, is described in the next chapter.

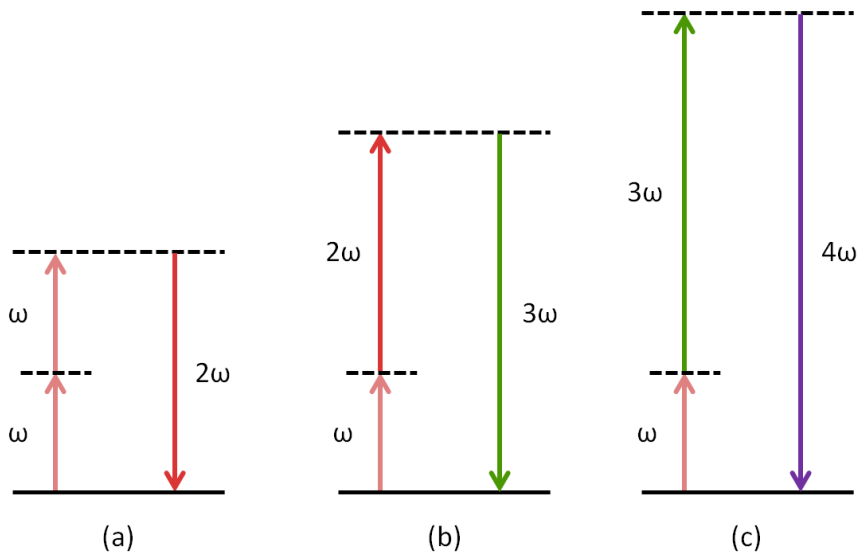

Figure 3.4: Energy level diagram for cascaded harmonic generation. The second harmonic (a) is added to the pump to produce a cascaded third harmonic (b), which is then added to the pump again to produce the fourth harmonic. This cascaded process is a combination of second harmonic and sum-frequency generation, and is therefore the result of only $\chi^{(2)}$ processes

3.3.4 $\chi^{(2)}$ and Noncentrosymmetric Media

It should also be noted that, although second order effects are typically much stronger than higher order effects, second order electric dipole processes can only occur in media that do not posess inversion symmetry. This result can be understood by considering the Lorentz model, which describes the interaction of electromagnetic fileds with atomic structure in terms of a harmonic oscillator, with the addition of nonlinearity in the restoring force (44).

The equation of motion for the electron position is

$$x'' + 2\gamma x' + \omega_0^2 x + ax^2 = \frac{-eE(t)}{m} \tag{3.13}$$

where $-e$ is the electron charge, m is the electron mass, E is the electric field, and

the damping force is assumed to be

$$-2m\gamma x' \tag{3.14}$$

then the restoring force on the electron is given by

$$F = -m\omega_0^2 x - max^2 \tag{3.15}$$

where a is proportional to the strength of the nonlinear response. Integrating this expression over x yields the potential energy function

$$U = -\left(\frac{1}{2}m\omega_0^2 x^2 - \frac{1}{3}max^3\right) \tag{3.16}$$

This expression represents a harmonic potential, with the second term on the right corresponding to an anharmonic deviation, as shown in Fig. 3.5. Physically, this anharmonic potential can be understood to describe a material in which the crystal lattice does not possess inversion symmetry, and so the potential experienced by an atomic electron is not exactly parabolic.

The major consequence of this requirement is that materials which do possess inversion symmetry, including gasses, liquids, amorphous materials (e.g. fused silica) and crystalline materials (e.g. silicon) will have no second order effects. In these cases, the lowest order nonlinear susceptibility will be $\chi^{(3)}$.

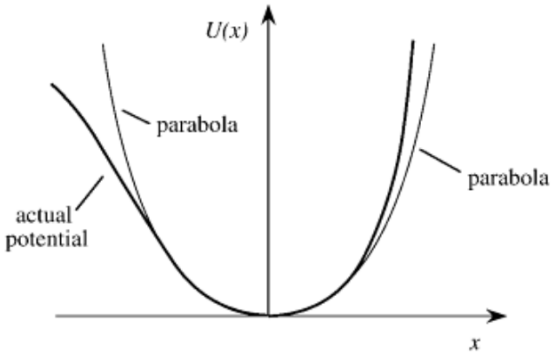

Figure 3.5: Representation of the potential energy function for a material without inversion symmetry, from (44).

3.3.5 Raman Scattering

An optical wave propagating in a crystal can also shift its frequency due to inelestic scattering from lattice vibrations, or phonons. Scattering from optical frequency phonons, known as Raman scattering, causes the optical wave to either gain or lose energy. In the case of a photon losing energy to a phonon, known as Stokes scattering, the crystal lattice is heated, and the optical signal is red-shifted. In the opposite process, anti-Stokes scattering, a photon gains energy from the lattice, cooling the material and blue-shifting the optical signal. Because the likelyhood of Raman scattering depends on the population of the initial phonon state, at thermodynamic equilibrium Stokes scattering will dominate.

In an additional processes known as hyper Raman scattering (45; 46), the energy from two pump photons is results in the creation of an optical phonon and a photon at nearly twice the pump energy. Figure 3.6 shows the energy diagram representation for Raman and hyper Raman scattering, which are $\chi^{(3)}$ nonlinear effects.

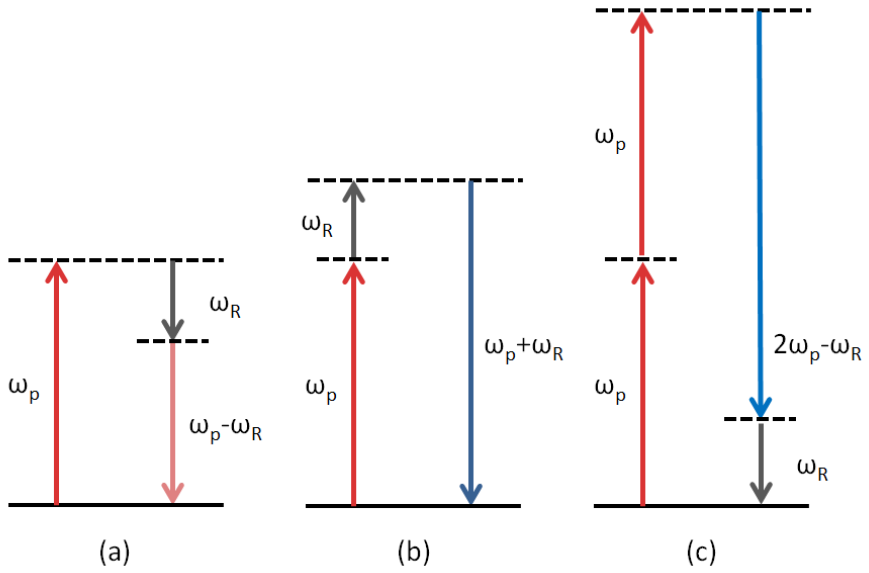

Figure 3.6: Energy level diagram for (a) Stokes and (b) anti-Stokes Raman scattering. In the Stokes process, energy from the photon is lost to an optical phonon, red-shifting the light. In the anti-Stokes process, the photon gains energy from a phonon, blue-shifting the light. In hyper Raman scattering (c) two pump photons are destroyed, and a photon at twice the pump energy minus the optical phonon energy is created

3.4 Nonlinear Materials

A wide variety of materials have been shown to exhibit useful nonlinearity. Some of these are useful as semiconductors or piezoelectrics, and many are commercially available with in bulk and wafer form with high purity. Some of the most important and commonly used second order nonlinear crystals are listed here:

- Lithium niobate ($LiNbO_3$)
- Lithium tantalate ($LiTaO_3$)
- Potassium niobate ($KNbO_3$)
- Potassium titanyl phosphate (KTP)
- β-barium borate (BBO)
- Gallium arsenide ($GaAs$)

Figure 3.7 and 3.8 show examples of lithium tantalate (47) and lithium niobate (48) in bulk and wafer form.

Figure 3.7: Single crystal lithium tantalate boules (47).

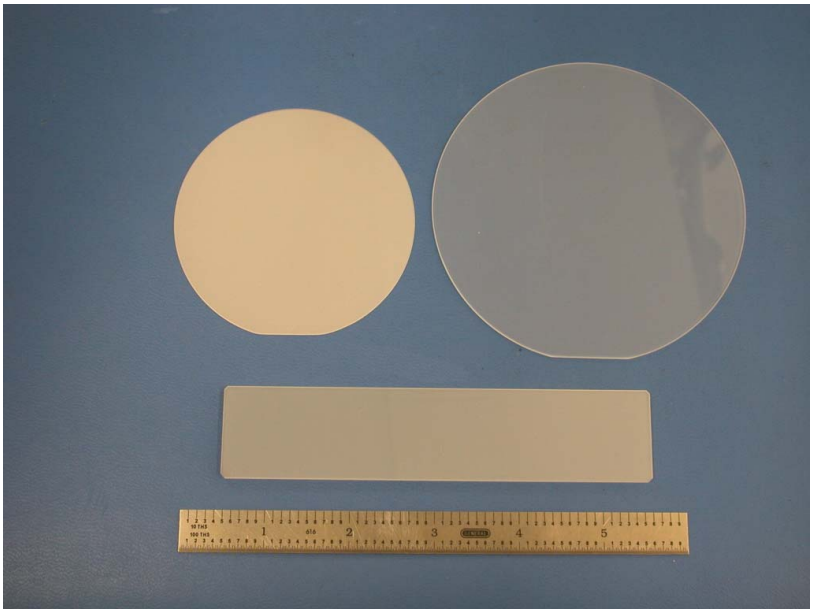

Figure 3.8: Lithium niobate bulk sample and wafers (48)

CHAPTER IV

Harmonic Generation in a Lithium Niobate Whispering Gallery Resonator

4.1 Introduction

Scaling of laser sources to shorter wavelengths is a challenging task. The required energy for a conventional laser scales as $1/\lambda^5$, where λ is the laser wavelength (43). There are, however, a wide range of applications for short wavelength lasers, including

- Industrial - micromachining, surface cleaning of materials, thin film sputtering
- Medical - corneal surgery
- Semiconductor - small feature size lithography
- Optics - writing fiber Bragg gratings

Harmonic generation is not subject to the same laser scaling limits, and is therefore a natural choice for extending the emission wavelength of a pump laser to produce coherent ultraviolet light, unrestricted by the $1/\lambda^5$ relation. However, to date such short-wavelength sources have required very high pump power levels that could generally be achieved only by ultra-short pump pulses (49; 50; 51; 52; 53). Resonant

enhancement is an alternative to ultra-short pump pulses for providing the high field intensities required for efficient nonlinear effects.

Whispering gallery resonators are simple, momolithic devices which can be used to greatly amplify the intensity of a continous-wave pump source. This is because high quality factor whispering gallery resonators enhance the intensity of light continuously in time via many recirculations, resulting in high finesse and large light-matter interaction distances (18; 19; 20).

In this work, we experimentally demonstrate continuous-wave harmonic generation up to the fourth harmonic, enabled by multiple recirculation intensity enhancement in a lithium niobate whispering gallery resonator. This could potentially transform high-harmonic studies from pulsed to continuous-wave. Specifically, we generate continuous-wave near infrared, visible, and ultraviolet light from a telecommunication-compatible infrared pump through cascaded harmonic generation in a whispering gallery resonator at a pump power of 200 mW (49; 50; 51; 52; 53). Further, our millimeter scale emitter is simple, as the polished lithium niobate resonator comprises both the nonlinear medium and the mode confining resonator. A nonuniform poling of lithium niobate (54) and existence of higher order transverse modes (33) provides the required quasi-phase matching between the infrared pump and the corresponding near infrared, visible, and ultraviolet harmonics.

Finally, multi-photon Raman scattering processes observed in the same system are discussed.

4.2 Finite Element Modeling

Although exact solutions exist for spherical geometry (39), whispering gallery modes of nonspherical systems require approximations or numerical simulation. Resonance calculation for the pump and corresponding harmonics of the lithium niobate disk is done using finite element method simulation in COMSOL Multiphysics. Al-

though a three dimensional analysis of whispering gallery modes is possible, the system under consideration is symmetric about the vetical axis. A 2D axial symmetric model is therefore used to reduce the computational intensity of the problem (38). Lithium niobate was chosen for our whispering gallery resonator nonlinear medium for its second order optical nonlinearity and its transparency from infrared to ultraviolet wavelengths. Additionally, due to its ferroelectric properties, lithium niobate crystal domains can be engineered by electrical poling to achieve quasi-phase matching of diverse nonlinear optical processes. Phase matching is discussed in more detail in following sections.

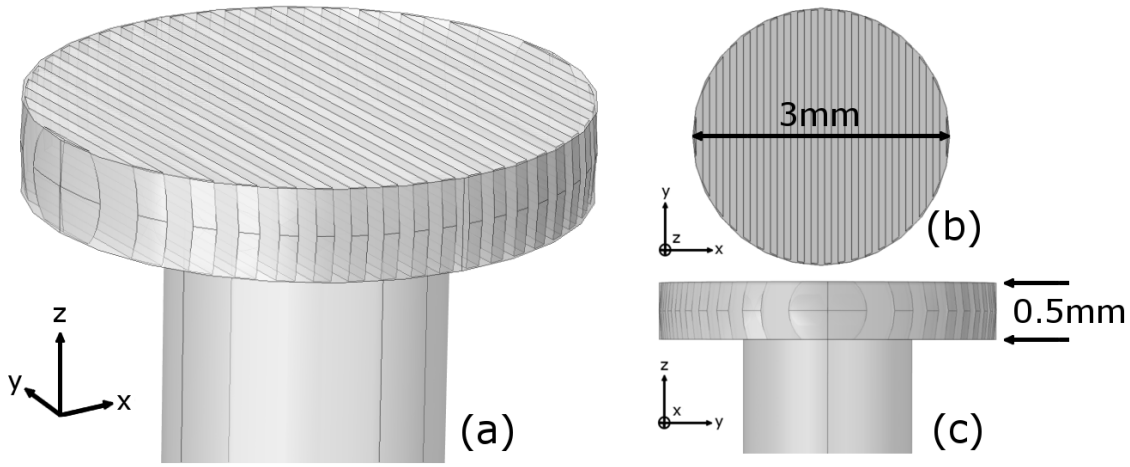

Figure 4.1: Schematic diagram of lithium niobate resonator. The disk is 3mm in diameter, 0.5mm thick, and has an approximately spherical curvature (i.e. the radius of curvature is equal to the disk radius)

The lithium niobate disk modeled in this analysis is 3mm in diameter and 0.5mm thick. The radius of curvature of the outside surface is nominally the same as the radius of the disk, and so the resonator approximates a 0.5mm thick section cut from the center of a sphere. A schematic diagram of the device is shown in Fig. A.1. Transverse electric (TE) modes are defined as those polarized in the z-direction, while

transverse magnetic (TM) modes are polarized in the xy plane. The optical axis of the crystal and the disk are the same, and so TE modes considered in this analysis "see" the extraordinary refractive index, while TM modes are subject to the ordinary refractive index.

Resonator modes for were calculated as described in (38), in COMSOL v.3.5. For a given azimuthal mode number m, electric field profiles and eigenfrequencies are obtained for the geometry described above with ordinary and extraordinary refractive indices according to (55). Table 4.1 shows the resulting calculated TE harmonic frequencies and refractive index data for a 1550nm pump.

Table 4.1: Calculated Pump and Harmonic Modes

Harmonic	Wavelength (nm)	Ord. index n_o	Ext. index n_e	Azimuthal mode number m	TE Frequency (Hz)
pump	1550nm	2.216	2.136	13430	1.935×10^{14}
2^{nd}	775nm	2.264	2.177	26479	3.877×10^{14}
3^{rd}	516.7nm	2.334	2.238	40752	5.802×10^{14}
4^{th}	387.5nm	2.517	2.359	57280	7.734×10^{14}

The calculated cross-sectional electric field profiles the pump and harmonic resonator modes are shown in Figure 4.2. The energy circulating in the infrared pump and the corresponding second (nearinfrared), third (visible), and fourth (ultraviolet) harmonic modes is located near the surface of the lithium niobate disk.

The electric field profiles of the modes along the resonator equator in the radial direction are shown in Figure 4.3. In smaller whispering gallery resonators, such as silica microspheres (10), a significant part of the mode volume can be found outside the resonator. However, as show in Figure 4.3, the modes in this system are confined almost completely inside the disk. This is due to the high refractive index of lithium

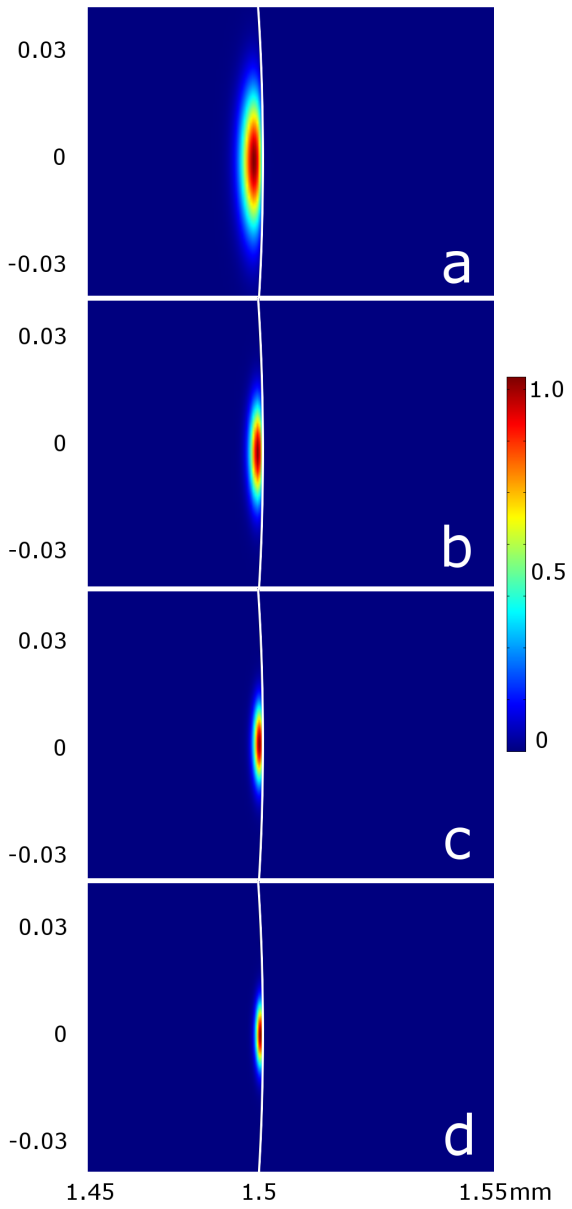

Figure 4.2: Electric field profiles for (a) pump (1550nm), (b) 2nd harmonic (775nm), (c) 3rd harmonic (516.7nm), and (d) 4th harmonic (387.5nm)

niobate and the relatively large size of the resonator compared with the pump and harmonic wavelengths.

To quantify the spatial overlap of the various modes, the parameter η is defined as

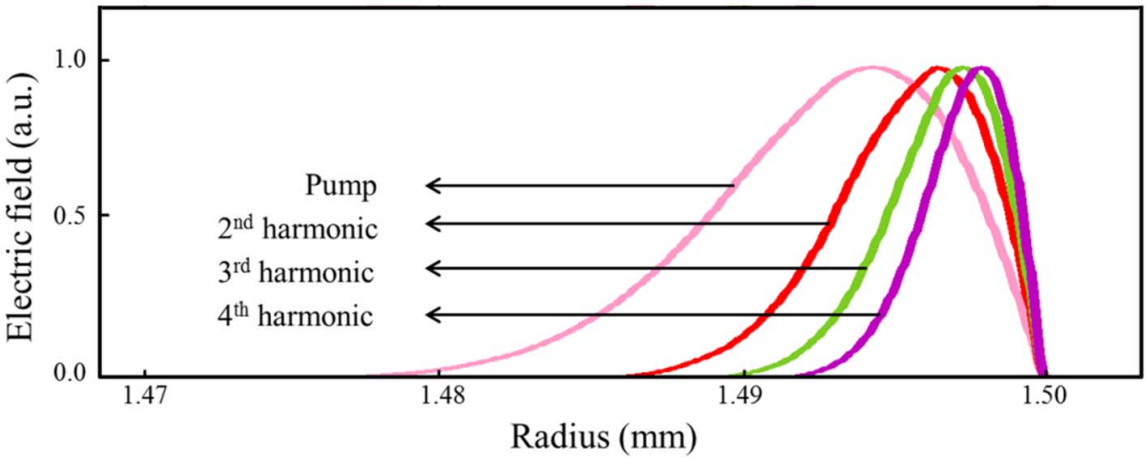

Figure 4.3: Electric field values for pump and harmonics as a function of radius, along the resonator center line $z = 0$

$$\eta_{i,j} = \frac{|\int E_i^* E_j dA|^2}{\int |E_i|^2 dA \int |E_j|^2 dA} \tag{4.1}$$

where i and j are indices representing the pump, second, third, and fourth harmonics. For example $\eta_{pump,2}$, the overlap between the pump and second harmonic is 0.7134. $\eta_{i,j} = 1$ signifies that the two modes overlap exactly, while $\eta_{i,j} = 0$ indicates complete spatial separation. Table 4.2 shows the value of $\eta_{i,j}$ for all combinations of pump and harmonic modes.

Table 4.2: Overlap Integral $\eta_{i,j}$ for Pump and Harmonics

i \ j	*pump*	2	3	4
pump	1.0	0.7134	0.4202	0.2374
2	0.7134	1.0	0.8702	0.6425
3	0.4202	0.8702	1.0	0.9143
4	0.2374	0.6425	0.9143	1.0

4.3 Phase Matching

4.3.1 Dispersion and Phase Matching

The modes are expected to resonate at integer multiples of the pump frequency, in order to conserve energy as required by coupled-mode theory (56). However, structural and material dispersion cause the propagation constants to be scaled differently as a function of frequency. This implies that momentum is not *a priori* conserved for the harmonic processes in the bare resonator.

As a result of the k-vector mismatch, the propagating optical wave does not maintain a fixed phase relation to the electric polarization wave, and so energy cannot be efficiently extracted from the pump. Another way to view this situation is that the signals generated in parts of the crystal where the waves are out of phase will simply transfer energy back to the pump, preventing efficient conversion to the generated frequency (44).

Phase matcing is the name for the group of techniques used to compensate for dispersion effects. Typically, phase matching techniques in $\chi^{(2)}$ nonlinear crystals exploit the birefringence of nonlinear materials, and the crystal is rotated to find an

orientation where the propagating pump and signal have the same refracitve index (57). Additionally, the birefringence of a crystal may exhibit temperature dependence, and so heating or cooling the material may achieve the same result.

Birefrigent phase matching may not always be practicle, however, due to device geometry, material properties, or other requirements. For some materials, including lithium niobate, quasi-phase matching can be used to compensate the negative effects of dispersion on conversion efficiency.

4.3.2 Quasi-Phase Matching

Birefringent phase matching techniques exploit the anisotropy of the crystal to create conditions where the pump and generated signal remain in phase. In some situations, this is not possible at convenient temperatures. There are also geometric concerns such as spatial walk-off, where the Poynting vector and the wavevector have different directions, causing a loss of energy from the nonlinear pocess, which limit the use of birefringenct phase matching. Quasi-phase matching compensates for dispersion effects by the periodic modulation of the material structure, and can be used to address some of these issues.

Unlike birefringent phase matching, quasi-phase matching does not lock the phase the interacting modes. Instead, the sign of the nonlinear coefficient is periodically reversed by modifying the material or structure, so that energy continues to transfer from pump to signal.

Figure 4.4 summarizes the three cases of phase matching. For the case of perfect phase matching, shown in Fig. 4.4(a), the waves are in phase and the generated intensity grows monotonically with propagation distance z. In 4.4(c), the waves are out of phase. The generated intensity grows over the first coherence length, but as the waves move out of phase, energy begins tranfering back to the pump. This process continues in a cycle, with energy flowing back and forth from pump to signal, and

efficient conversion is not achieved. In 4.4(b), the sign of $\chi^{(2)}$ has been reversed each integer number of z/L_{coh}, and so although the pump and signal do not propagate in phase, energy is efficiently transfered to the generated wave.

The most common quasi-phase matching technique is known as periodic poling, in which the spontaneous polarization of a ferroelectric crystal is periodically reversed by the application of a large voltage across the crystal. Lithium niobate is one of the most common materials which is periodically poled for quasi-phase matching.

The optimum poling period for each three-photon interaction harmonic generation process is given by

$$\Lambda = \left(\frac{n_1}{\lambda_1} + \frac{n_2}{\lambda_2} - \frac{n_3}{\lambda_3} \right)^{-1} \tag{4.2}$$

where λ_1 and λ_2 are the wavelengths of the input photons, λ_3 is the wavelength of the generated photon, n_1 and n_2 are the mode indices of the input photons and n_3 is the mode index of generated photon.

Domain reversal is achieved by the application of a large voltage across the sample, approximately 20kV/mm. Periodically poled lithium niobate (PPLN) wafers are available commerically, and our resonator is fabricated from such a wafer (54; 38; 56; 58).

In contrast to the typical case of straight propagation through a bulk sample of nonlinear media, the modes of a whispering gallery resonator propagate in a circle with respect to the poling domains. A circularly symmetric resonator can be poled in a variety of configurations (54), two of the simplest of which are shown in Fig. 4.5. As shown in the figure, a propagating mode in a radially poled resonator (Fig. 4.5 (a)) will experience a uniform poling period, while a mode propagating in a stripe poled resonator (Fig. 4.5 (b)) will experience a nonuniform poling period.

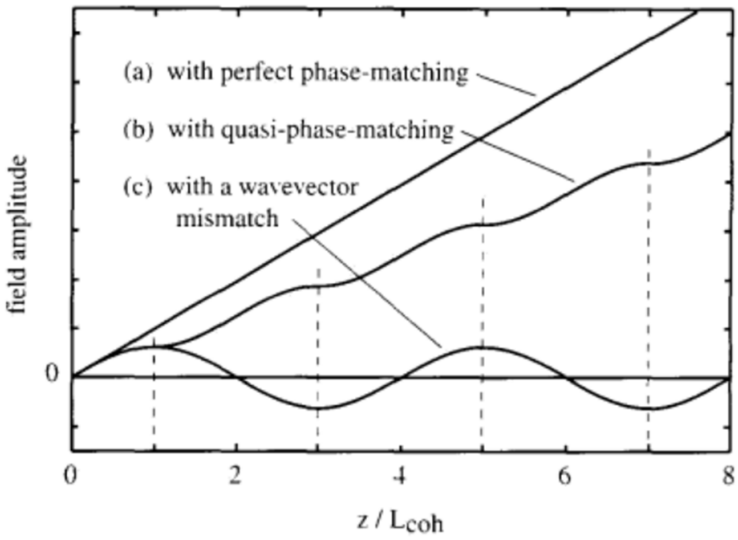

Figure 4.4: Conversion efficiency for (a) perfectly phase matched (b) quasi-phase matched and (c) not phase matched processes(44)

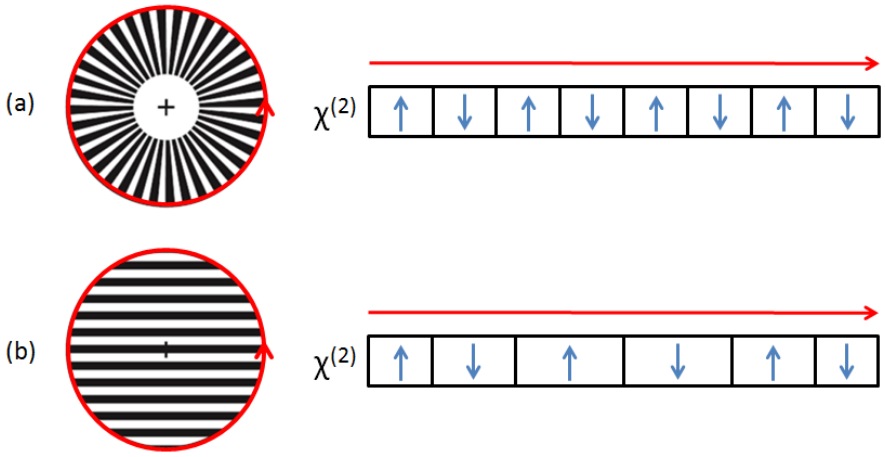

Figure 4.5: Propagation of a whispering gallery mode through (a) radial and (b) striped poling configurations. The mode sees a uniform poling period in the radial case, and a nonuniform poling period in the striped case.

A major challenge in quasi-phase matching cascaded interactions is that different poling periods are required to compensate for the momentum mismatch of different

nonlinear processes. This means that fixing the poling period to optimize a particular nonlinear process will not, in general, allow for efficient quasi-phase matching of the remaining processes. For example, the optimal poling periods for second, cascaded third, and cascaded fourth harmonic generation for a 1550nm pump in lithium niobate are 19μm, 7μm, and 2.13μm, respectively.

Plotting the envelope function of the Fourier coefficients for the poling pattern seen by the azimuthally propagating mode provides information about the relative efficiency of phase matching for different processes (58). The efficiency of a given nonlinear process is directly proportional to amplitude of the Fourier coefficient at the optimum poling period for that process.

Figure 4.6 shows the amplitude of the Fourier coefficients as a function of inverse grating period for our 3mm diameter resonator with 79μm striped poling, confirming that the quasi-phase matching condition can be partially satisfied for all three harmonic-generation processes simultaneously.

It should be noted that although the relative quasi-phase matching efficiency of the three processes discussed here differ by less than an order of magnitude, poling configurations with shorter periods will have a much better phase matching performances for all processes than the PPLN wafer available for this experiment. While these results effectively demonstrate a proof of concept, we anticipate that shortening the grating period will greatly improve efficiency in future devices.

4.3.3 High Order Modes

In addition to periodic poling, the existence of high order modes facilitates phase matching over a broad pump wavelength range (33; 59; 16). In the previous section, only first order modes of the resonator were considered. However, because of the large size and broad curvature of the resonator, a large number of high order modes are supported by the structure. The effective refractive indices for these modes can

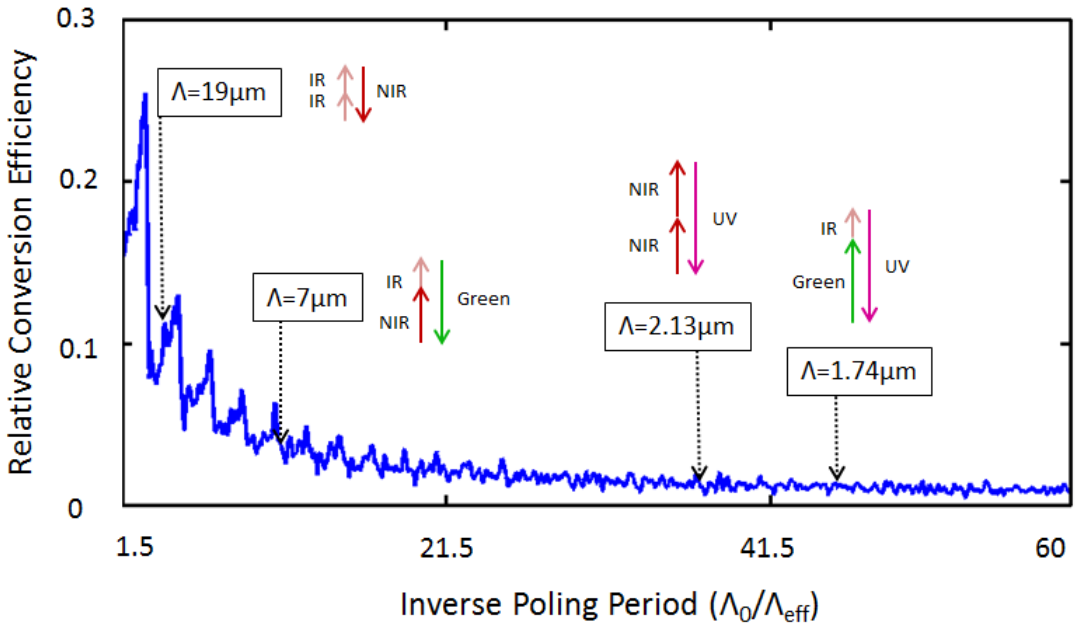

Figure 4.6: The amplitude of the Fourier coefficients for the poling pattern seen by the azimuthally propagating mode, for our 3mm diameter resonator with $\Lambda_0 = 79\mu m$ striped poling, confirming that the energy-momentum condition can be satisfied for all three harmonic-generation processes simultaneously

differ significantly from each other, and so coupling to these higher order modes can relax the phase matching requirements (33; 59). As shown in later sections, coupling to high order modes also allows tunability of the harmonic generation process.

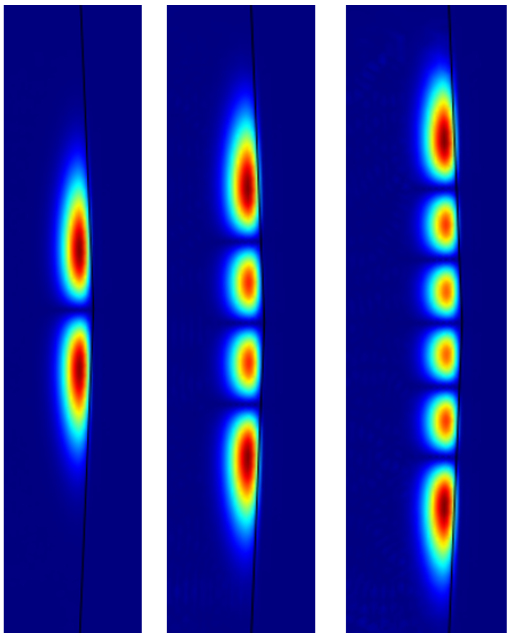

Figure 4.7: COMSOL simulation showing high order transverse optical modes of the lithium niobate disk. High order modes assists periodic poling with phase matching

4.4 Fabrication

The resonator used in these experiments was fabricated from a commercial z-cut, periodically poled lithium niobate wafer. The original two inch wafer (0.5mm thick) was diced into 5 × 5mm squares. The squares were then mounted on an air bearing spindle (Fig. 4.8), rough cut to 3mm diameter circular disks, and the edges were mechanically hand polished with a graded series of alumina polishing grit. The fabrication of the first devices was accomplished with assistance from Opticology, Inc. (NY). A finished device, mounted on a brass support, is also shown in Fig. 4.8.

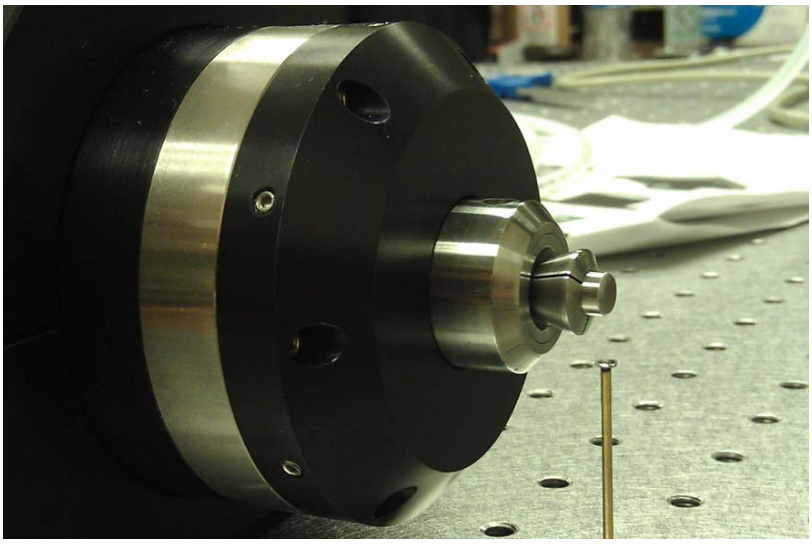

Figure 4.8: Air bearing spindle of the type used to hand polish lithium niobate whispering gallery resonator.

4.5 Prism Coupling

Laser light is evanescently coupled to the cavity modes via a prism (60). Prism coupling is one of several well establised technique for coupling energy to whispering gallery modes, as well as for extracting signals from the resonator. Tapered fiber coupling was deemed inappropriate in our case due to the high refractive index of the resonator ($n_r \simeq 2.2$).

The most important concern for coupling efficiently to the device is matching the momentum of the resonator mode with the effective propagation constant in the prism. Figure 4.9 describes the coupling geometry. The laser enters the prism with wavevector k_i and refracts from the first interface before being totally internally reflected from the surface next to the resonator. In order to match the propagation constant β for the reflected wave with the wavevector inside the resonator k_r:

$$\beta = k_r = k_p sin\theta_p \tag{4.3}$$

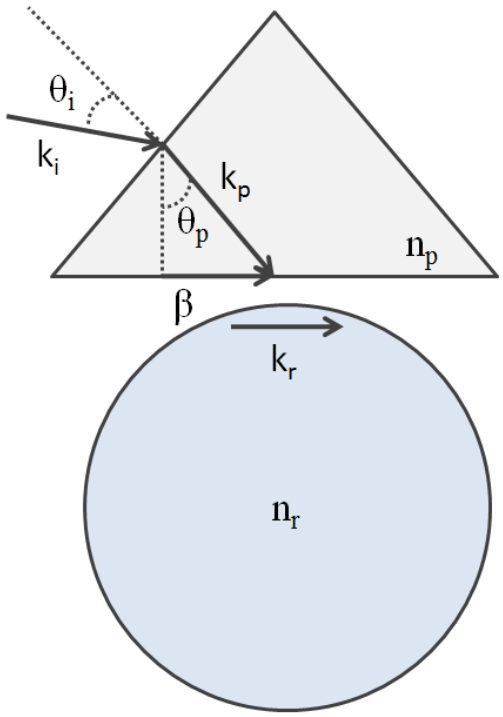

Figure 4.9: Diagram of momentum matching requirements for prism coupling to lithium niobate whispering gallery resonator.

For the geometry shown in Fig. 4.9 and a 60° angle prism, the required angle of incidence for the incoming beam θ_i, relative to the normal of the first prism face, is given by

$$\theta_i = sin^{-1}\left(n_r\frac{\sqrt{2}}{2} - \frac{\sqrt{2}}{2}n_p cos\left(sin^{-1}\frac{n_r}{n_p}\right)\right) \tag{4.4}$$

One important consequence of Eq. 4.3 is the requirement

$$n_r = n_p sin\theta_p \tag{4.5}$$

which implies that the prism refractive index must be higher than the resonator index

$$n_p > n_r \tag{4.6}$$

Resonant modes of our 3mm lithium niobate resonator have a refractive index around $n = 2.2$, depending on polarization and mode profile. This limits the possible materials for the prism. A few possible high index prism materials for coupling infrared light are

- Rutile (TiO_2)
- Zince Selenide ($ZnSe$)
- Diamond

Diamond was chosen as the prism material due to its transparency over the ultraviolet to infrared range, its lack of birefringence, and its relatively low dispersion. Diamond is not a common material for most optical components, and so a custom prism was ordered. The dimensions of the prism, grown by chemical vapor deposition and polished by Element Six (Cambridge, MA), are shown in Fig. 4.10.

Figure 4.11 shows a plot of the coupling angle θ_i, including material dispersion, for a lithium niobate resonator, assuming the the effective mode index in the resonator is simply given by the bulk extraordinary refractive index of lithium niobate. The input angle for coupling light into the resonator is only a few degrees removed from

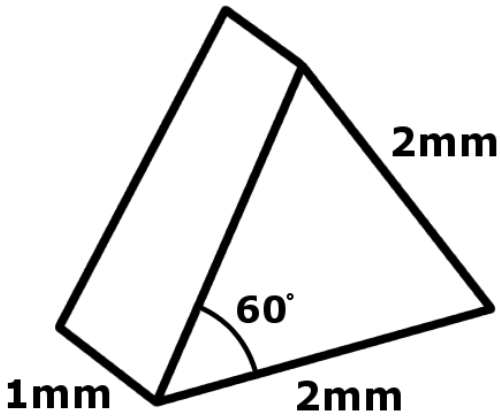

Figure 4.10: Dimensions of CVD diamond prism coupler

normal incidence. It should be noted that Fig. 4.11 also describes the angles at which light will couple out of the prism from the opposite face. As shown in the figure, the harmonics will be spatially separated from each other and the pump at the outcoupling facet.

While prism coupling is a widely applied technique, experimental realization is not necessarily straightforward, and several practical difficulties were encountered in the course of coupling to our device. The major difficulty was aligning the system to produce correct spatial overlap of the pump laser with the resonator mode. Because small deviations in the coupling angle, beam focus, and polarization can reduce the coupling efficiency, resonances were not initially observed in the transmission spectrum through the prism (as described in following sections). Without observation of resonance, it is difficult to ensure that the reflected pump beam spot on the coupling surface is properly aligned with the point of contact with the resonator.

The solution to this problem was to use an imaging technique to observe the point of contact between the resonator and prism, shown in Fig. 4.12. A microscope

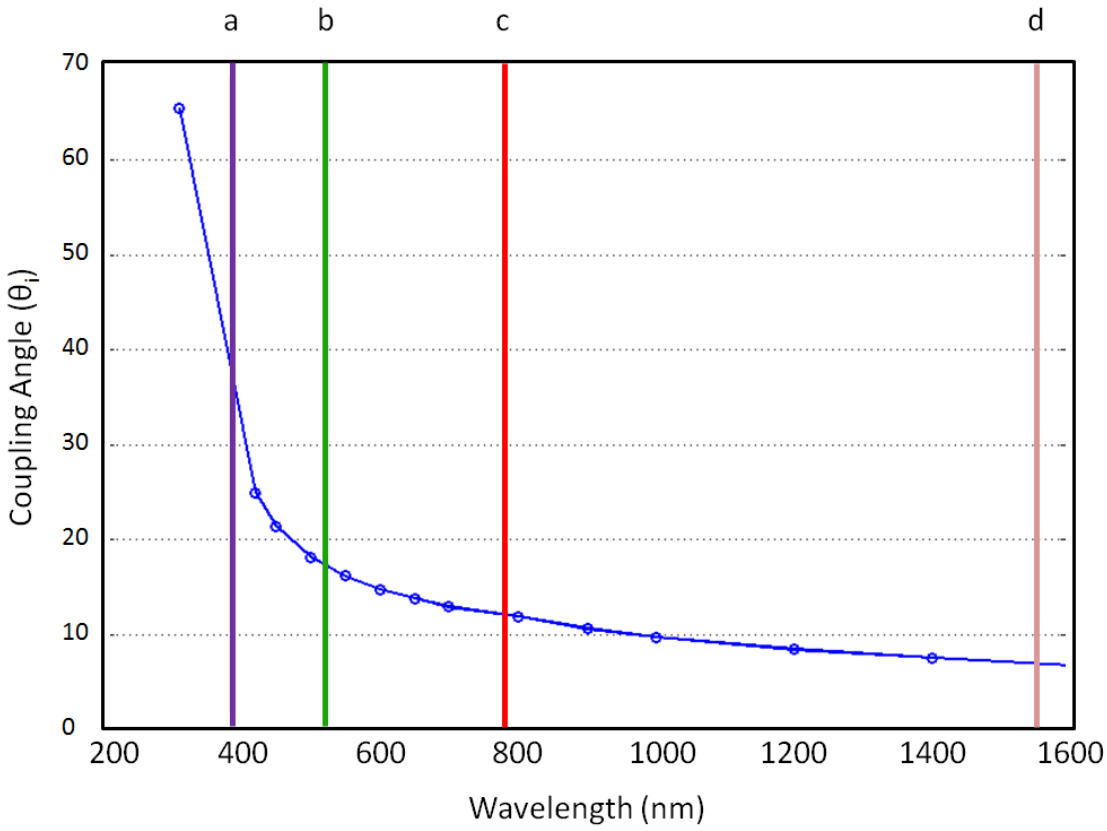

Figure 4.11: Coupling angle θ_i as a function of wavelength for diamond prism, assuming the resonator index is the bulk extraordinary index of lithium niobate. The colored bands show the locations of the (a) fourth (b) third and (c) second harmonics, as well as the infrared pump (d)

attached to an infrared CCD camera was used to image the facet of the prism in contact with the resonator. When a curved object touches a flat surface, interference patterns known as Newton's rings are created. Moving the laser systematically across the surface of the prism, several such ring patterns were observed, some of which were interpreted as dust particles on the prism surface. However, the ring pattern created by the contact point between the resonator and prism was observed to dissappear when the resonator was moved back from the prism, and so this method established the correct alignment of the beam with the resonator. Subsequent adjustment of

focus, angular alignment, tilt, and polarization of the source were then carried out in order to optimize coupling.

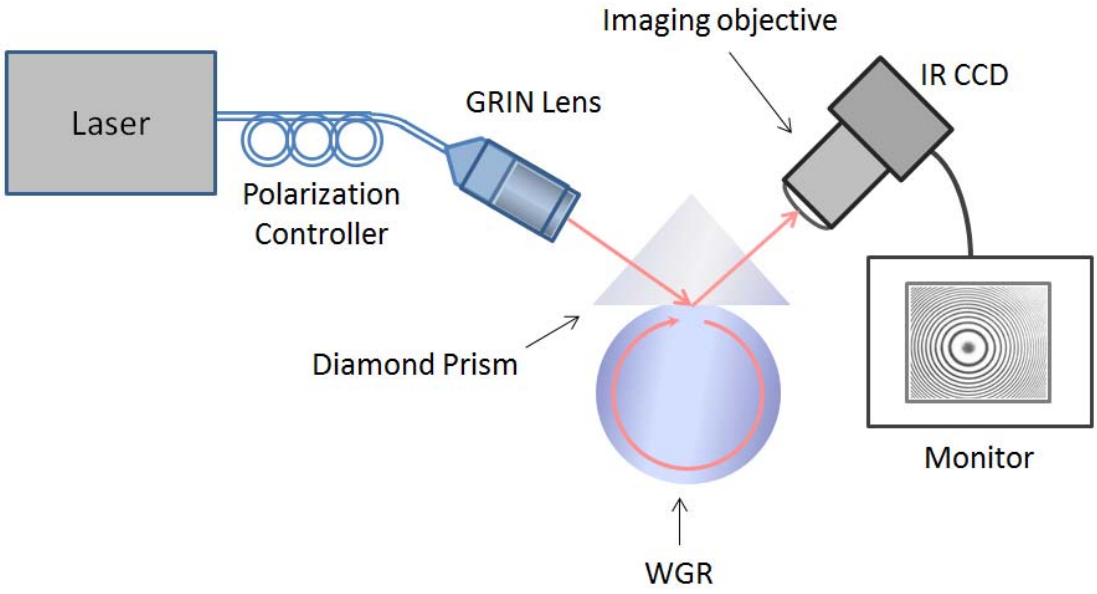

Figure 4.12: Diagram of experimental setup used to establish prism coupling to whispering gallery modes. A microscope focused on the coupling face is used to observe Newton's rings created by interference at the contact point. This allows correct alignment of the coupling beam with the resonator

A photgraph of the diamond prism and the resonator, with the resonator slightly backed away from the coupling position, is shown in Fig. 4.13.

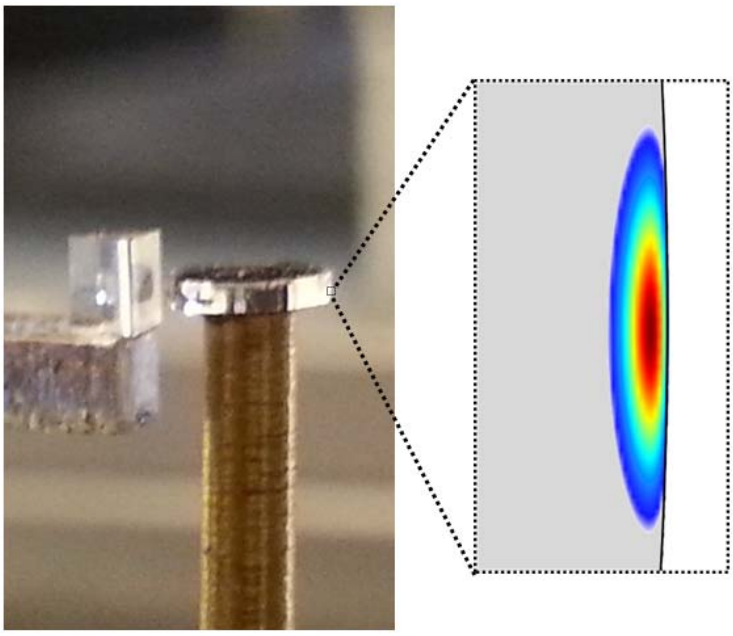

Figure 4.13: Photograph of diamond prism and resonator with superimposed electric field profile calculated in COMSOL.

4.6 Experimental Results and Discussion

The experimental setup for demonstrating cascaded harmonic generation in the resonator is shown in Fig. 4.14. The pump beam, tunable from 1535 to 1545nm, is evanescently coupled into the resonator, and emitted light is coupled out via the prism, where it is observed on a CCD camera. Emitted light is also collected in a multimode fiber from Rayleigh scattering from the surface of the disk, and anaylzed on a series of spectrum analyzers spanning the ultraviolet to infrared (Ocean Optics Maya 2000Pro, Ocean Optics USB4000, and HP 8565E). A photograph of the experimental setup is shown in Fig. 4.15.

Third harmonic generation in the resonator is visible as bright green light emitted from the disk surface. Although the second harmonic is more intense, the sensitivity of the human eye and the CCD camera used in the experiment is much higher around

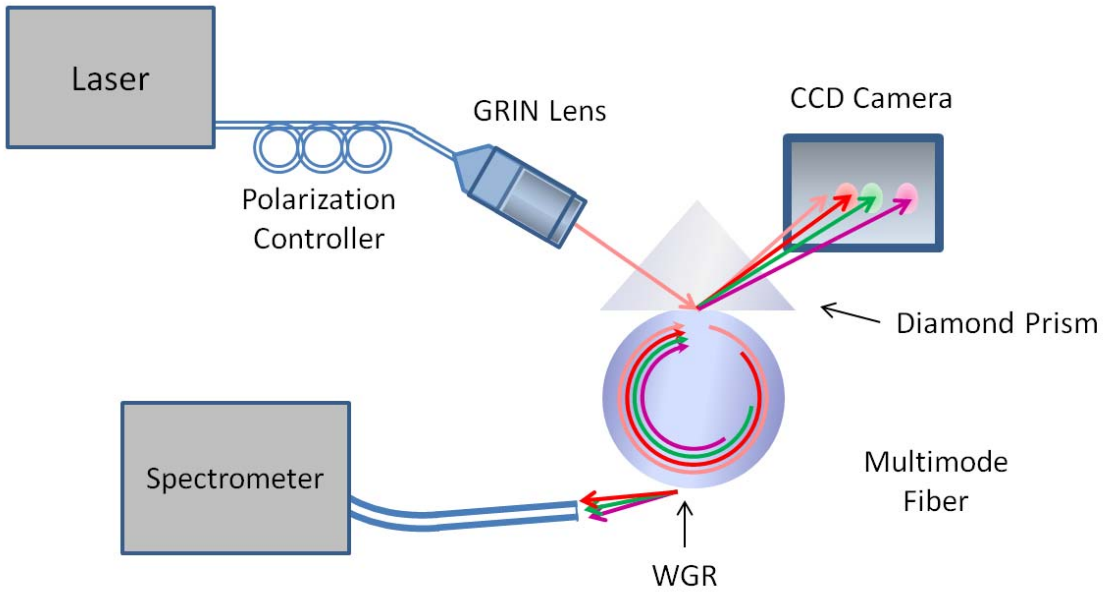

Figure 4.14: Experimental setup for demonstrating cascaded-harmonic generation in the periodically poled lithium niobate resonator.

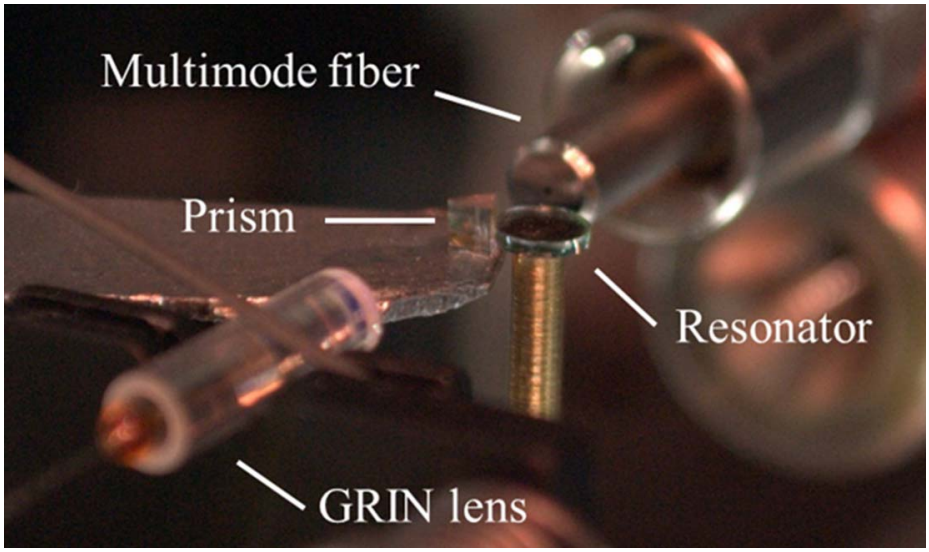

Figure 4.15: Photograph of experimental setup.

515nm than at 773nm, which is in the near infrared. Consequently, the third harmonic is more evident to photographic observation. Figure 4.16 shows a photograph of green emission with an infrared pump via cascaded third harmonic generation.

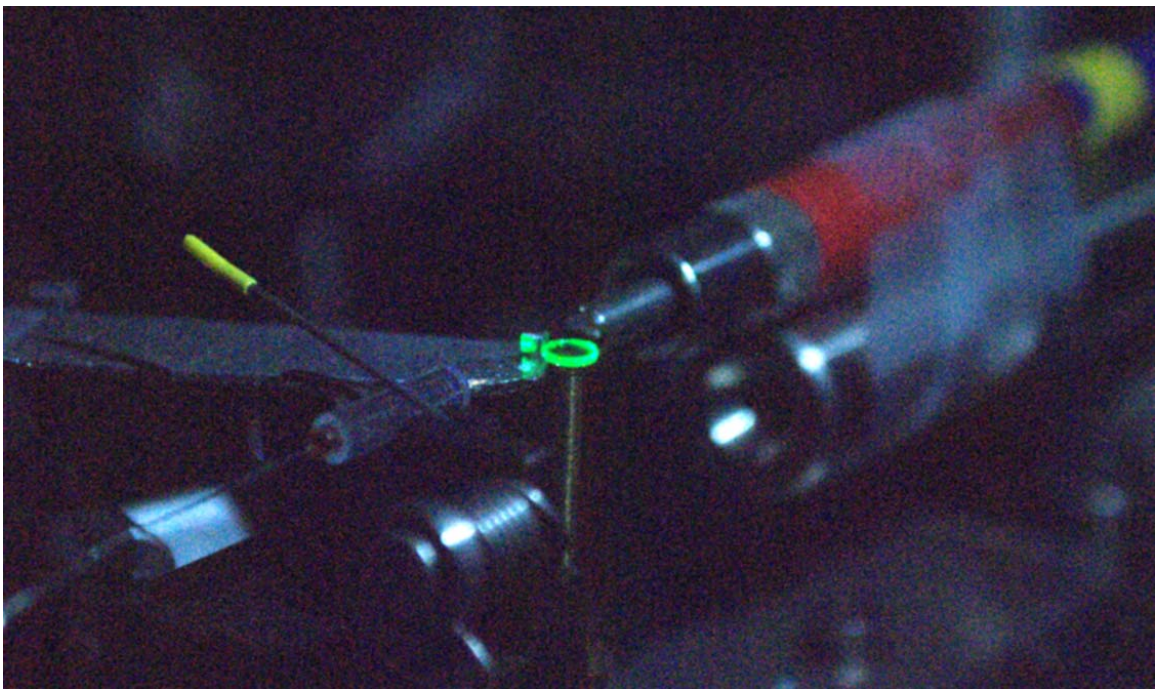

Figure 4.16: Photograph of green emission from the resonator via cascaded third harmonic generation. The infrared pump and near infrared second harmonic are not visible due to the greater sensitivity of the camera to visible wavelengths.

4.6.1 Quality Factor

The quality factor of resonator modes was determined using the experimental setup in Fig. 4.17. Scanning the pump laser wavelength reveals transmission dips at resonant frequencies, as shown in Fig. 4.18. The measured free spectral range of the resonator is 9.3GHz.

The quality factors of resonator modes can be found from the width of the trans-

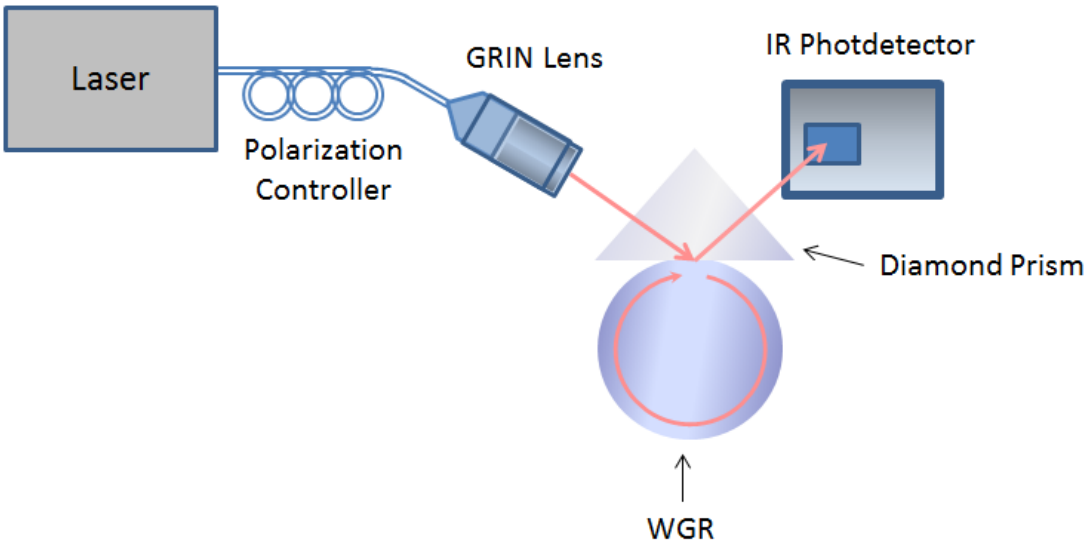

Figure 4.17: Experimental setup for measuring resonator quality factor. The laser wavelength is tuned, and the transmission through the prism is recorded on an infrared photodetector. Resonator modes are observed as dips in the transmission spectrum.

mission dips:

$$Q = \frac{f_0}{\delta f}, \tag{4.7}$$

Q values as high as 2×10^7 were measured for the pump wavelength in the lithium niobate disk, as shown in Fig. 4.19.

Measuring the quality factor in the ultraviolet is challenging because of the lack of narrow linewidth tunable lasers for the UV band, as well as the lack of spectrum analyzers with resolution in the order of 10MHz. Compared to the IR pump, absorption losses for the UV fourth harmonic will be higher in lithium niobate. However, loss via tunneling (10) decreases at shorter wavelengths. Additionally, quality factor

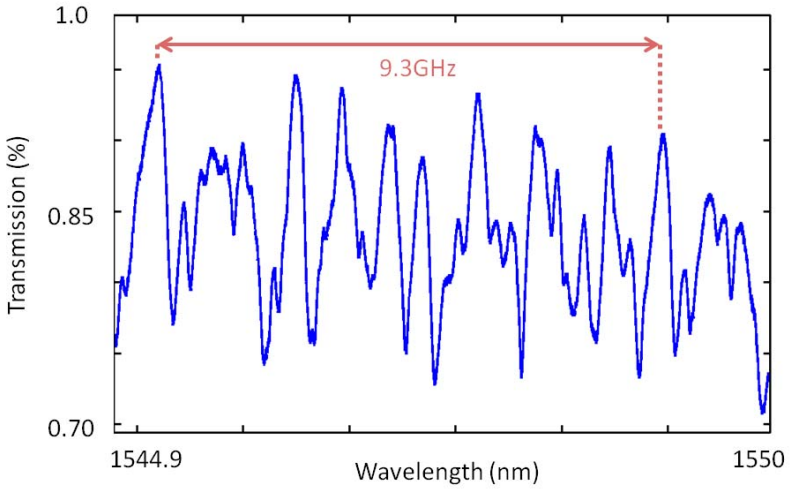

Figure 4.18: Transmission spectrum of the pump laser measured at the output of the diamond prism. The free spectral range of the resonator is measured to be 9.3GHz, with maximum coupling efficiency around 30%

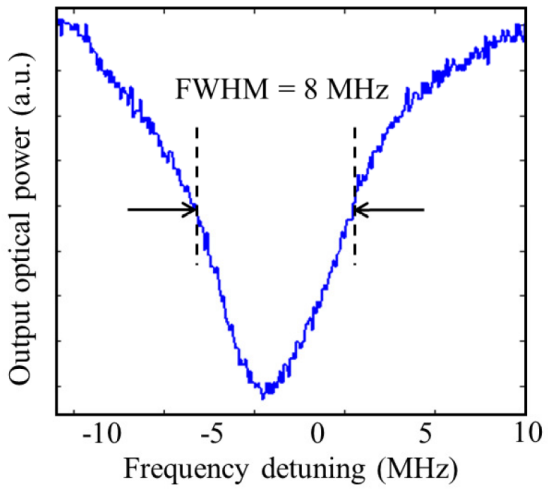

Figure 4.19: High-Q pump resonance measurement. The corresponding Q value is 2×10^7

is inversely proportional to wavelength, assuming other losses are held constant. We therefore estimate that Q for the fourth harmonic is of the same order as for the IR pump. Also, the power used in this experiment is not high enough to distort the Lorentzian shape of the absorption line, indicating a lack of thermal bistability in this experiment (61).

4.6.2 Harmonic Imaging

Experimental visualization of the cascaded harmonic generation process is achieved by photographing spatially resolved spots on a color and infrared CCD camera, with spot separations corresponding to the infrared pump and its second, third, and fourth harmonics (Fig. 4.20). Spectral filters are employed to prevent saturation of the camera by the second and third harmonics, and the fourth harmonic is observed by coating the CCD with a fluorescent ink that is sensitive to ultraviolet. The noncircular shape of the spots suggests that high order transverse modes are involved in this process. This image describes a continuous-wave emission for all of the generated harmonics.

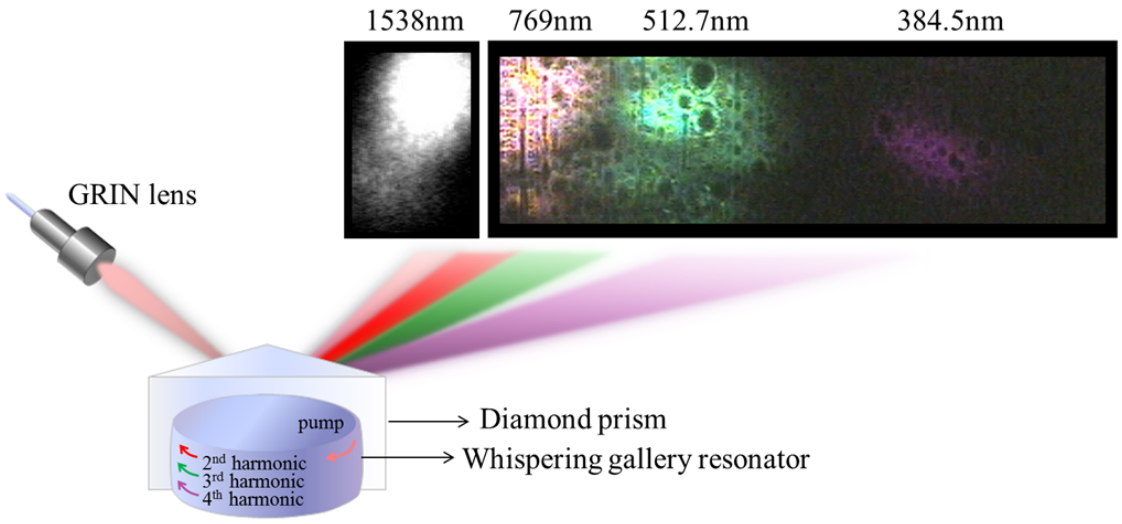

Figure 4.20: Visual verification of cascaded-harmonic generation: The pump beam is recorded with an infrared CCD camera, and the harmonics are observed on a color CCD coated with ultraviolet fluorescent ink. The photograph is taken at a pump wavelength of 1538 nm and a pump power of 200mW.

4.6.3 Emission Spectrum

Measuring the harmonics wavelengths is done by three spectrum analyzers which cover the infrared to ultraviolet band. The n^{th} harmonic is expected to be at the (pump wavelength)/n. The experimentally measured second, third, and fourth harmonic lines for the pump wavelength of 1546nm are at 773nm, 515nm, and 387nm, respectively (Fig. 4.21. These measured wavelengths lay within the 2nm error margin of our spectrum analyzers.

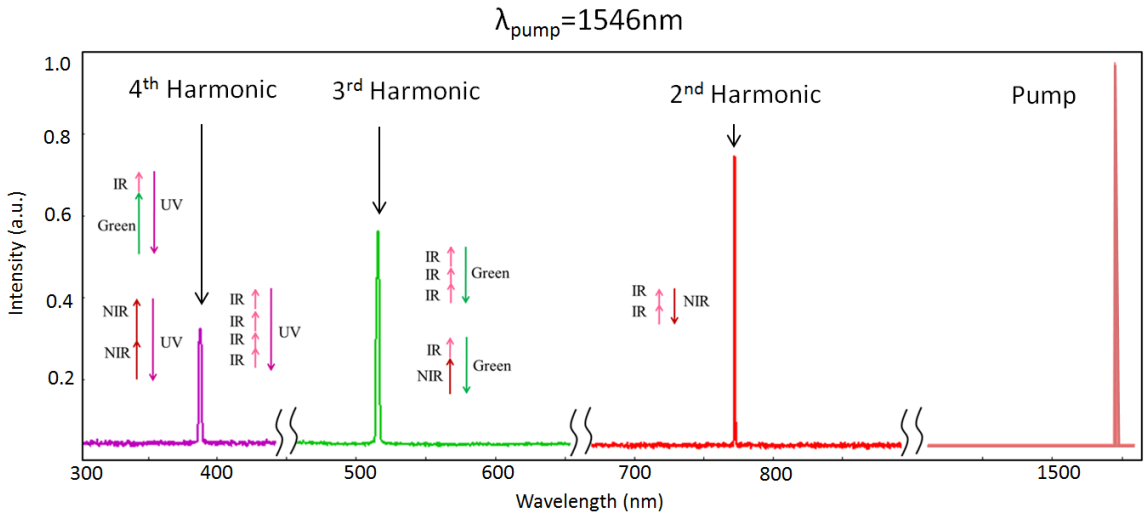

Figure 4.21: Measured emission spectrum at 1546nm pump wavelength, indicating generation of the second, third, and fourth harmonics at 773, 515.3, and 386.5nm, respectively. Harmonics are measured using two different spectrum analyzers, which together span the entire wavelength range, and are plotted at different intensity scales.

4.6.4 Harmonic Tunability

Tuning the harmonics wavelengths is possible in our experimental setup by sweeping the pump wavelength through the very dense infrared resonance modes of the whispering gallery resonator to reveal a nearly continuous tuning capacity. We experimentally demonstrate continuous tuning of the second, third, and fourth harmonic wavelengths while sweeping the pump wavelength between 1535nm and 1545nm (Fig. 4.22). All three harmonic wavelengths are observed to track the expected values as the pump wave length is varied.

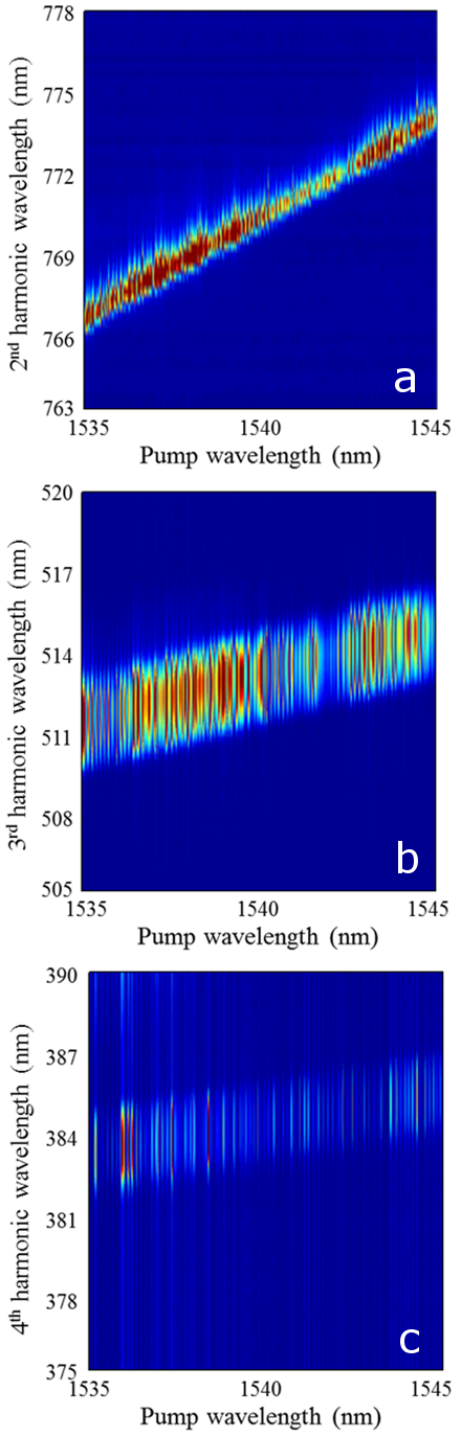

Figure 4.22: Measured spectrograms of the generated second (a) third (b) and fourth (c) harmonics at a pump wavelength range of 1535-1545nm. All three harmonics display wide tunability within this wavelength range

4.6.5 Power Dependence

Measuring the harmonics power as a function of the input pump power is performed to confirm the cascaded harmonic generation process. Inherently, the n^{th} harmonics power should scale as $(pump\,power)^n$, which is verified via a logarithmic fit of the second, third, and fourth harmonic power as a function of the pump power level (Fig. 4.23). This measurement was done by scanning the pump wavelength through several whispering gallery resonances to record an average output power for each harmonic at a given pump power. As it is evident from the measured harmonic powers, the cascaded harmonic process improves its efficiency as pump power increases. This is expected from the $(pump\,power)^n$ scaling of the n^{th} harmonic power. This efficiency will, of course, stop increasing when limiting effects such as pump depletion become evident, and can be limited by other considerations, including phase matching.

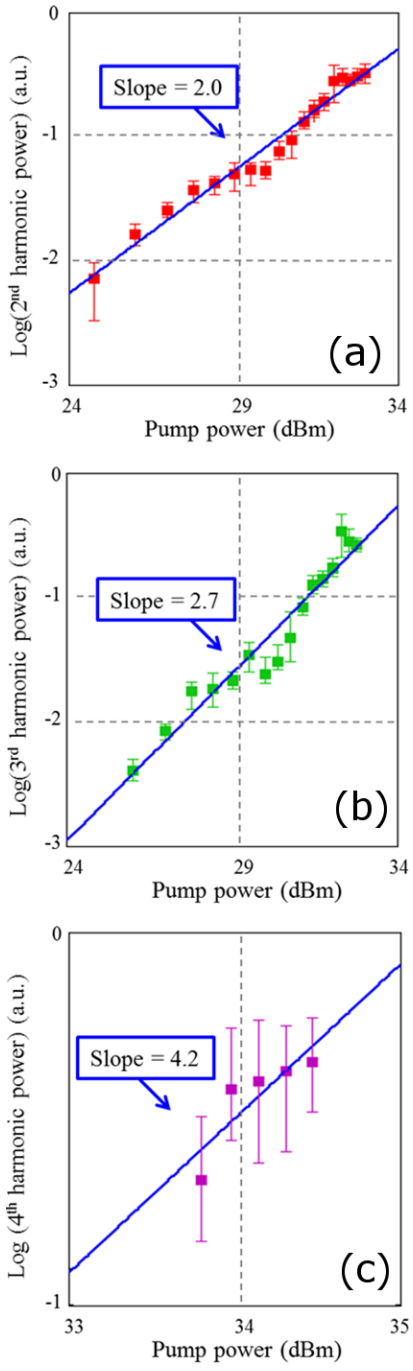

Figure 4.23: Measured power of the generated (a) second (b) third and (c) fourth harmonics at a pump wavelength of 1550nm, as a function of the pump power. Approximately quadratic, cubic and power-of-4 dependency are observed.

4.6.6 Cascaded Processes

We suggest that the mechanism responsible for the observed harmonic generation is cascaded harmonic generation via $\chi^{(2)}$ processes. This is because the third harmonic is only observed simultaneously with the second harmonic. Similarly, the fourth harmonic is only observed simultaneously with both the second and third harmonics. This suggests that the third and fourth harmonics arise from cascaded $\chi^{(2)}$ processes, as opposed to $\chi^{(3)}$ and $\chi^{(4)}$ effects. This observation is further supported by the fact that third and fourth order nonlinear coefficients are many orders of magnitude smaller than the second order coefficient for lithium niobate (44). In order to further validate the effectiveness of the employed quasi-phase matching technique, a second lithium niobate whispering-gallery resonator with no crystal poling was fabricated and tested using the same experimental setups. Harmonic generation was not observed in the similar experimental conditions, confirming the significant role of the employed non-uniform poling in providing quasi-phase matching for second, third, and fourth harmonic generation processes.

Additional evidence of cascaded $\chi^{(2)}$ processes could be obtained by excitation with circularly polarized light. In addition to linear photon momentum $\hbar k$, angular momentum ($\pm\hbar$) must also be conserved. For $\chi^{(3)}$ third harmonic generation, the circularly polarizd amplitudes of the generated signal are give by (62; 63)

$$E_{3\omega}^{\pm}(r) \sim E_{\omega}^{\pm}(0)^2 E_{\omega}^{\mp}(0) \tag{4.8}$$

where $E_{\omega}^{+}(0)$ and $E_{\omega}^{-}(0)$ are the left and right circular polarized field amplitudes, respectively, of the incident pump. Because both pump terms must be nonzero third harmonic conversion, the third harmonic cannot be generated with circularly polarized light. The observation of a third harmonic under circular polarized exitation

would confirm the observation of $\chi^{(3)}$ effects in the resonator, while its abscence would support the conclusion that cascaded $\chi^{(2)}$ effects are solely responsible for the observed harmonic generation.

4.7 Multi-Photon Raman Lasing

The cascaded harmonic generation processes observed in the resonator are also accompanied by stimulated Raman, two-photon, three-photon, and four-photon Raman scattering corresponding the molecular vibrational wavenumbers 632 and $255cm^{-1}$. Cominations of the harmonic frequencies and Raman frequencies, either through sum frequency generation or hyper-Raman scattering, yield many generated lines near the observed harmonics.

Figure 4.24 shows a stimulated Raman line at 1599nm which corresponds to the molecular vibrational wavenumber of $255cm^{-1}$ in z-cut lithium niobate crystal (60; 64; 65; 66). A second stimulated Raman line corresponds to the other molecular vibrational wavenumber of z-cut lithium niobate crystal at $632cm^{-1}$ and is not directly observed due to the limitation of the employed infrared spectrum analyzer. However, the proof of excitation of this Raman line is evident through several multi-photon Raman lines observed in the near-infrared, visible, and ultraviolet wavelength ranges.

More specifically, for a pump photon energy of $\hbar\omega_P$, the observed mid-infrared spectral lines (Fig. 4.25) at 824 and 851nm match with the two-photon Raman lines

$$2\omega_P - \omega_{R1} - \omega_{R2}$$

$$2\omega_P - 2\omega_{R2}$$

where $\hbar\omega_{R1}$ and $\hbar\omega_{R2}$ are the phonon energies of the 255 and $623cm^{-1}$ Raman lines, respectively.

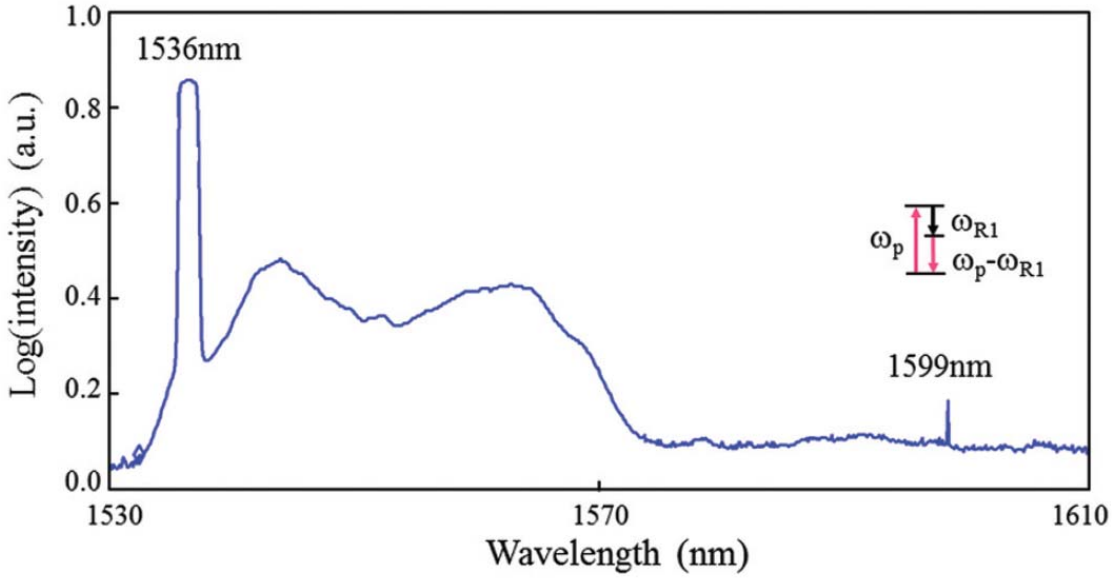

Figure 4.24: Measured emission spectrum of the whispering-gallery resonator at the pump wavelength of 1536 nm and pump power of 200 mW at infrared. The nearest Raman scattering line at $255cm^{-1}$ is recorded, along with the pump signal. A second stimulated Raman line corresponds to the other molecular vibrational wavenumber of z-cut lithium niobate crystal at $632cm^{-1}$ and is not directly observed due to the limitation of the employed infrared spectrum analyzer.

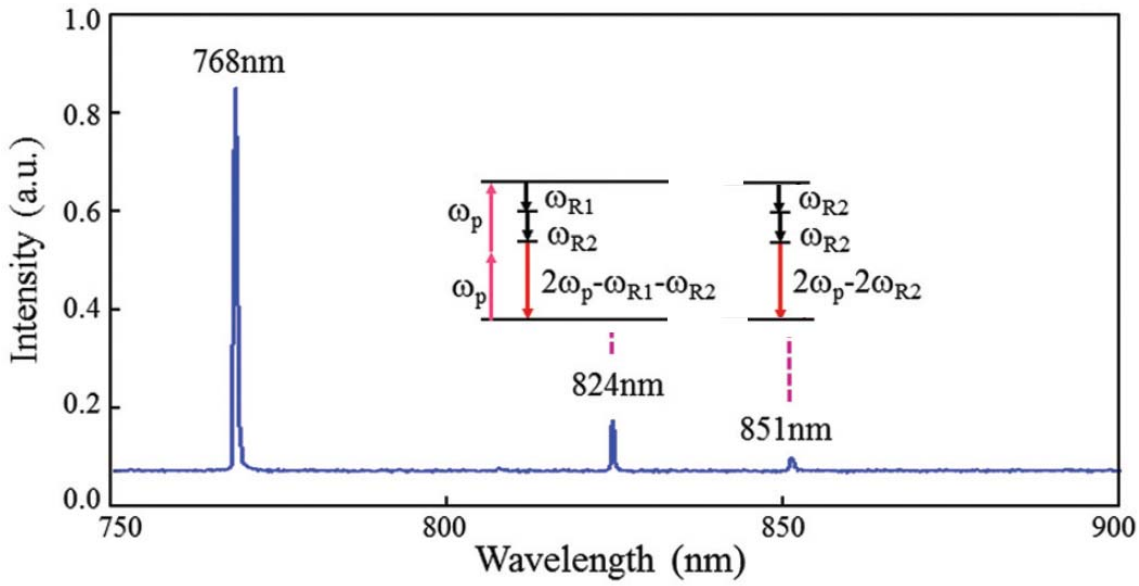

Figure 4.25: Measured emission spectrum of the whispering-gallery resonator at the pump wavelength of 1536 nm and pump power of 200 mW at the near infrared. The second harmonic is observed at 768nm with two additonal generated wavelengths at 824 and 851nm.

Similarly, the observed visible spectral lines near the third harmonic (Fig. 4.26) at 529, 536, 547, 567, and 588nm match with the three-photon Raman lines

$$3\omega_P - \omega_{R2}$$

$$3\omega_P - \omega_{R1} - \omega_{R2}$$

$$3\omega_P - 3\omega_{R2}$$

$$3\omega_P - 4\omega_{R2}$$

Although hyper Raman scattering (45; 46) is not observed in Fig. 4.25, the measured frequency $3\omega_P - \omega_{R2}$

at 529nm, shown in Fig. 4.26, shows a simultaneous interaction of three pump photons with a single optical phonon.

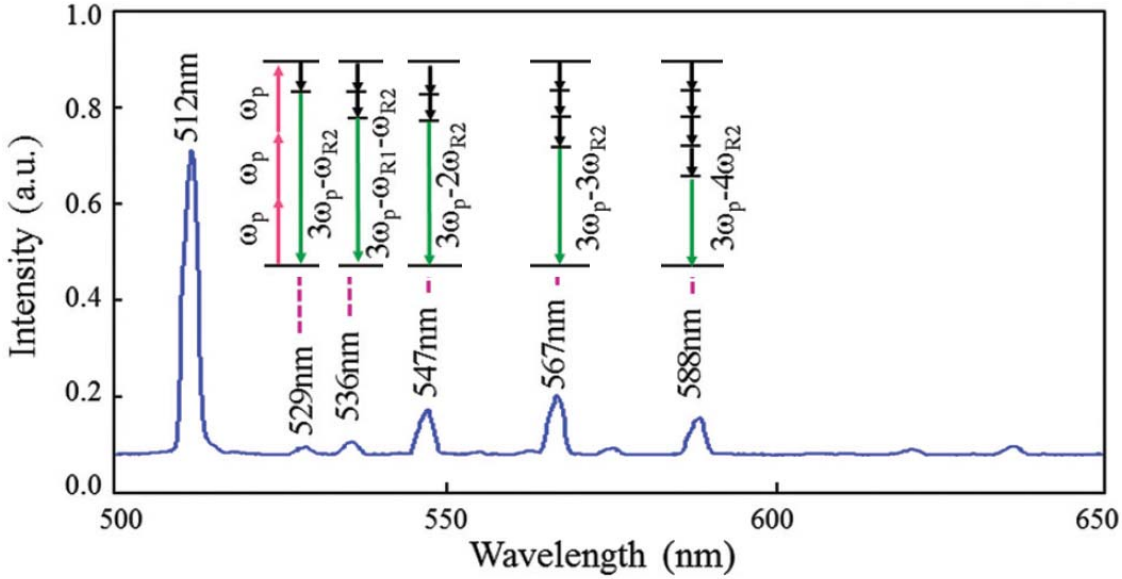

Figure 4.26: Measured emission spectrum of the whispering-gallery resonator at the pump wavelength of 1536 nm and pump power of 200 mW at the near infrared. The third harmonic is observed at 512nm with additonal generated lines at longer wavelengths.

The observed ultraviolet spectral lines are shown in Fig. 4.27 at 375, 393, 397, 404, 414, 419, 425, 430, 437, 449, 462, 468, and 476nm match with the four-photon Raman lines

$$4\omega_P + \omega_{R2}$$

$$4\omega_P - \omega_{R2}$$

$$4\omega_P - \omega_{R1} - \omega_{R2}$$

$$4\omega_P - 2\omega_{R2}$$

$$4\omega_P - 3\omega_{R2}$$

$$4\omega_P - \omega_{R1} - 3\omega_{R2}$$

$$4\omega_P - 4\omega_{R2}$$

$$4\omega_P - \omega_{R1} - 4\omega_{R2}$$

$$4\omega_P - 5\omega_{R2}$$

$$4\omega_P - 6\omega_{R2}$$

$$4\omega_P - 7\omega_{R2}$$

$$4\omega_P - \omega_{R1} - 7\omega_{R2}$$

$$4\omega_P - 8\omega_{R2}$$

We believe that both hyper-Raman (67) and cascaded Raman processes (28) are involved in the observed multi-photon Raman scattering that extends the spectrum of the pump and the second, third, and fourth harmonics to a train of lines that are separated by ω_{R1} and ω_{R2}.

4.8 Conclusion

In conclusion, we experimentally demonstrate continuous-wave cascaded harmonic generation up to the fourth harmonic in a millimeter-scale whispering gallery res-

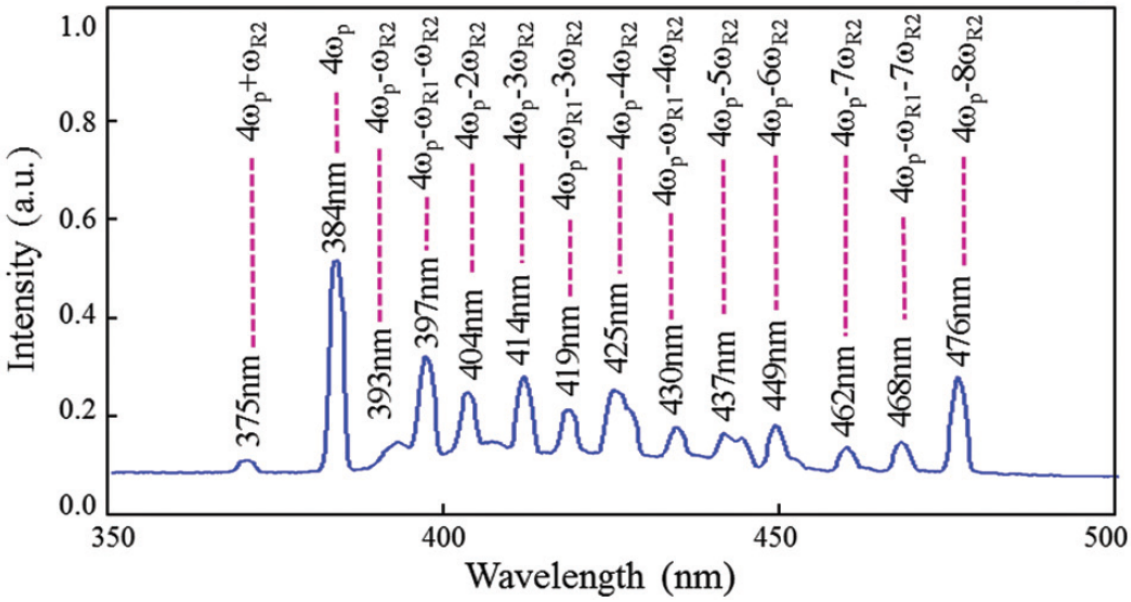

Figure 4.27: Measured emission spectrum of the whispering-gallery resonator at the pump wavelength of 1536 nm and pump power of 200 mW at the near infrared. The fourth harmonic is observed at 384nm with additonal generated wavelengths.

onator, allowing four spectral lines which are equally spaced in frequency and span a 2-octave frequency band. Many challenges exist, but we believe this work can be extended toward continuous-in-time extreme nonlinear optics where the electron is repeatedly torn from and recombines with the atom. These challenges include phase matching and concentration of light in the gaseous region near the evanescent tail of the modes discussed here. Still, the first steps in this journey, demonstrated here, can be followed toward the extreme by adding structures such as in (68) as suggested in (69).

CHAPTER V

Optical Trapping and Binding

This chapter provides an introduction to optical trapping. The methods of trapping and manipulating microscopic objects using laser light are explained. Also discussed is optical binding, the light-mediated interactions that occur when multiple objects are confined to the same optical trap.

5.1 Optical Trapping

5.1.1 History

The study of the mechanical forces exerted by light has had important implications for a wide range of scientific fields. Topics ranging from optical the manipulation of single cells in biology (70) to the creation of high frequency mechanical oscillators (10; 17) to laser cooling of solids (71) have been transformed by an improved understanding of the mechanical influence of light.

One important manifestation of these mechanical forces is the physical manipulation of dielectric objects by laser light, first shown by Ashkin at Bell Laboratories in 1970 with the trapping of micron scale latex spheres in a liquid medium with an argon laser beam (72). Optical trapping is possible in a variety of experimental configurations, and has been used extensively in biology and chemistry as a means of nondestructively manipulating microscopic objects (73). So-called optical tweezers

have been used to study a range of properties of microscopic objects, including bacteria, DNA molecules, and cell membranes (73; 74). One of the most basic optical trapping geometries is the single beam optical trap shown in Figure 5.1.

5.1.2 Optical Forces

There are two major forces which influence the optical manipulation of small objects. The first of these, the gradient force, exists for objects with a higher refractive index than the surrounding material. For nanoscale objects, the gradient force can be understood as the creation of an induced electric dipole in the object, and the action of the focused beam's gradient force on this dipole. The object will be drawn into the center of the beam, which represents a potential energy minimum for the dipole. For objects larger than the wavelength, the gradient force can be examined with geometric optics. As shown in Figure 5.1, the light rays refracting through a dielectric sphere experience a change in momentum, which results in a force toward the center of the beam.

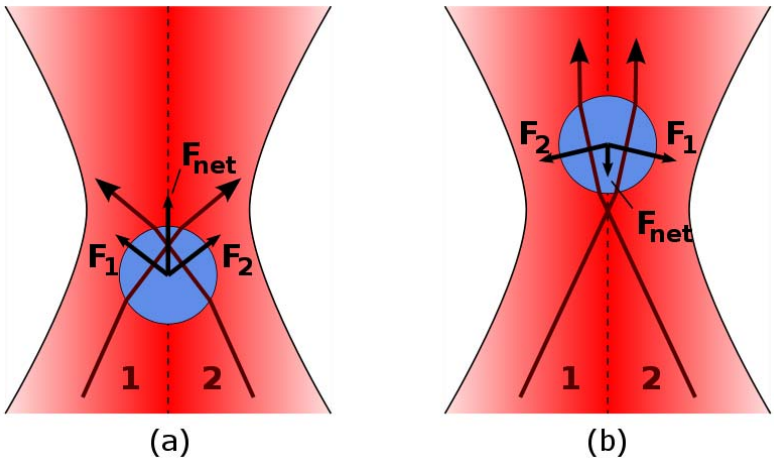

Figure 5.1: Gradient force optical trap. Lensing of tightly focused Gaussian beam creates forces which pull the dielectric sphere into the beam's intensity maximum

The other important force in optical trapping experiments is the scattering force. This force results from the scattering of photons from the object, and so it points in the direction of beam propagation. In single beam trapping experiments with a tightly focused beam, the scattering force will cause the object to be displaced slightly beyond the focus of the beam. For a weakly focused beam, shown in Figure 5.2, the scattering force can be balanced by the force of gravity to trap an object vertically. Horizontal confinement is still the result of the gradient force.

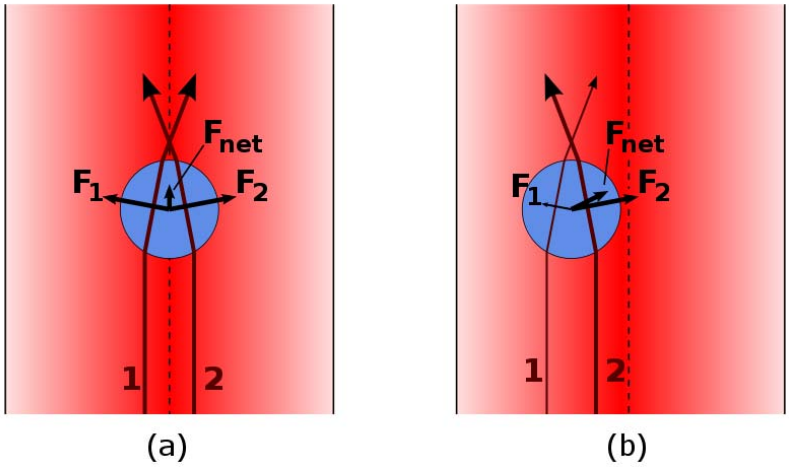

Figure 5.2: Optical trap with a weakly focused optical beam. Confinement in the vertical direction is primarily a result of balancing the optical scattering force upward with the force of gravity downward. Confinement in the lateral direction is product of the gradient force, just as in the tightly focused beam trap

For a weakly focused trap, the scattering force can be calculated as

$$F_s = Q\frac{nP}{c} \tag{5.1}$$

where P is the beam power, n is the refractive index of the surrounding medium, and c is the speed of light. Q is a dimensionless parameter determined experimentally.

In a vertical beam trap, this force must balance gravity. For a spherical dielectric object, the gravitational force is given by

$$F_g = g\frac{4}{3}\pi r^3 \rho \tag{5.2}$$

where g is acceleration due to gravity, r is the sphere radius, and ρ is the material density. As an example, the trapping forces for for fused silica microspheres in air, with $0.2 < Q < 1$, trapping powers are in the range of a few tens of milliwatts. While these powers are easily accessible with commerical lasers, trapping much larger objects becomes challenging, due to the the r^3 dependence of the trapping power.

5.2 Optical Binding

Trapping multiple objects can be achieved by creating multiple potential wells with holographic techniques (75; 76) or by time sharing of a single laser (77). In some cases, however, multiple objects are confined to a single trap, resulting in light mediated interaction of trapped objects, known as optical binding (78; 79; 80).

Optically bound objects interact with each other through scattering of the light, forming a variety of one, two, and three dimensional static and dynamic configurations. The first observed cases of optical binding were 2D interactions of dielectric spheres in liquids. Initially, an intensity pattern formed by interfering multiple beams was used to assemble crystal structures with trapped polystyrene spheres, shown in Figure 5.3. However, similar behavior was observed when the sample cell was illumninated with a single Gaussian beam that was more than 10 times the diameter of the spheres.

This self-assembly of trapped objects is attributed to the interaction of trapped particles through the scattering of light and has been reported with a variety of media

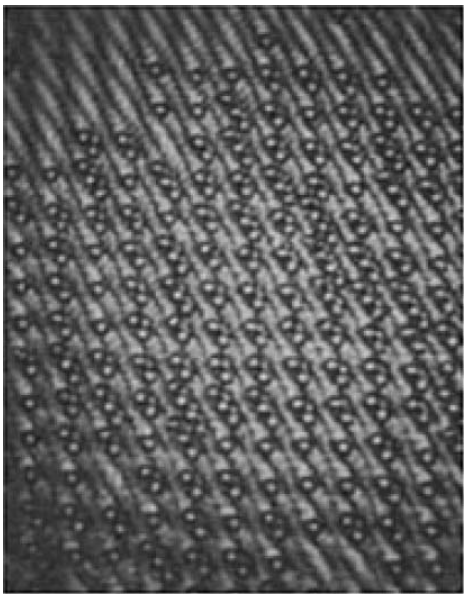

Figure 5.3: Opticaly trapped polystyrene spheres. Interference of the trapping beams produces a periodic trapping potential, resulting in 2D "crystal" structure against the top of the sample cell

and configurations. Figure 5.4 shows three examples of groups of optically trapped objects in air.

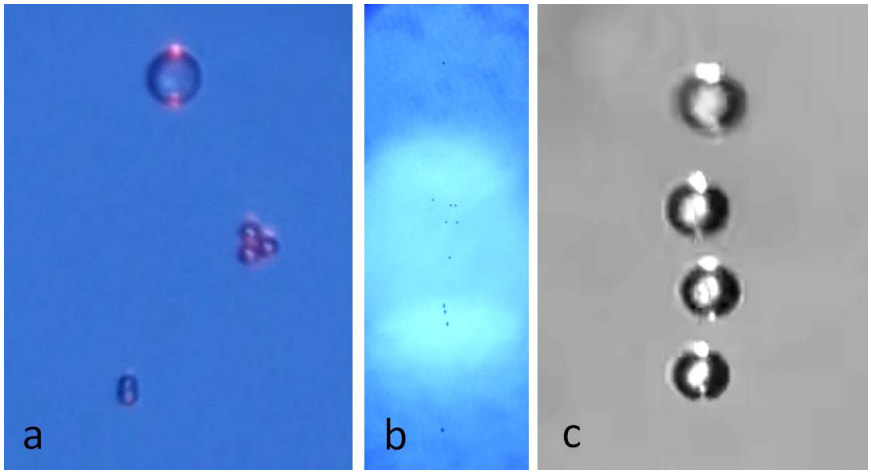

Figure 5.4: Configurations of optically trapped silica microspheres in a single Gaussian beam trap. (a) Three trapped objects, both spherical and nonspherical, formed from $7\mu m$ and $25\mu m$ diameter microspheres (b) 11 trapped objects (c) four trapped $25\mu m$ silica spheres

Since it's discovery, optical binding has been investigated in a variety of media, size regimes, and confiurations. The final chapter of this work describes the investigation of optically bound fused silica objects in air.

CHAPTER VI

Long-Range Optical Binding of Aerosols

This chapter describes the experimental demonstration of long-range, underdamped otpical binding of aerosols. The experimentally observed behavior and interaction of objects confined to the same optical potential well trap are discussed.

6.1 Introduction

Interaction of trapped particles with each other, mediated by light, is sometimes observed in optical traps. These processes, referred to as optical binding (78), have received significant attention in recent years (79; 80). Pioneering work in optical clustering in air includes one dimenstional clustering of aerosols which cling weakly to interference fringes in an optical trap (81; 82). It is natural to try and cluster matter in light when the bare optical trap is smooth and has only one weak local minimum. In this work we investigate an optical trap that is much larger than the aerosol. The trap contains a single weak potential minimum, in which multiple aerosols cluster while interacting with the electromagnetic field to produce additional minima.

6.2 Experimental Results and Discussion

6.2.1 Methods

Our experimental setup (6.1) uses of a tunable 1.5μm laser coupled to a single-mode optical fiber as suggested in (80) for shaping the beam to prevent transverse irregularities in the trap. Outside the fiber, the beam is weakly focused through a graded index lens to create a vertical single potential-well trap in air. The trap contains no counter propagating beam, so that there are no interference fringes and the trap is smooth along the propagation direction of the light. We suspend silica particles in a size range from 7 to 25μm and monitor them using a microscope.

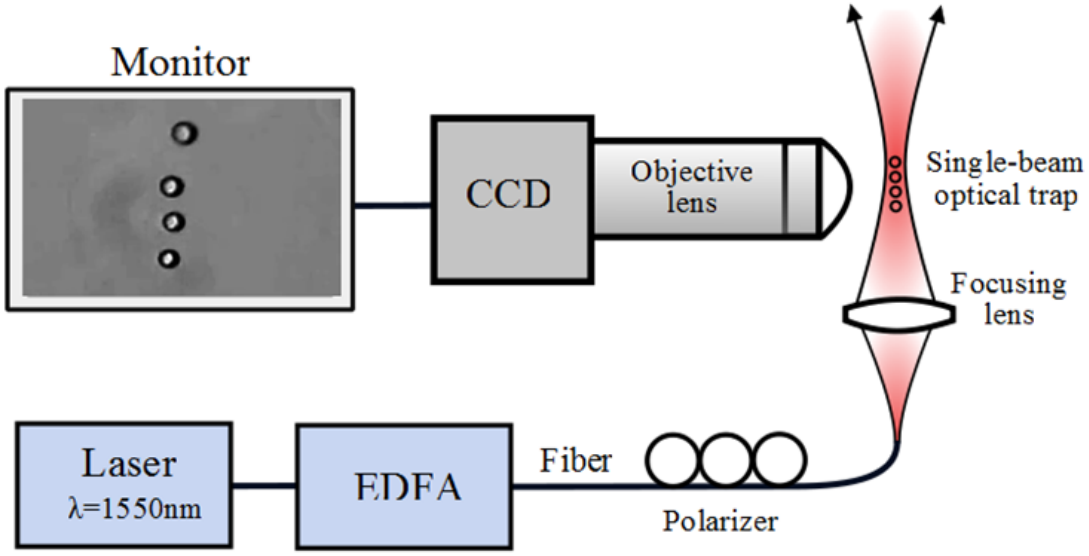

Figure 6.1: Experimental configuration for single beam optical trap. Microspheres are dispersed by compressed air in the vicinity of a weakly focused, single-beam optical trap

Additionally, a low power red laser can be used to illuminate the trap for imaging purposes. The red laser also aids in the recording of glare points at the microsphere

azimuths, caused by excitation of confined whispering gallery modes, described previously (81). Four trapped silica microspheres, nominally 25μm diameter are shown with glare points in Figure 6.2.

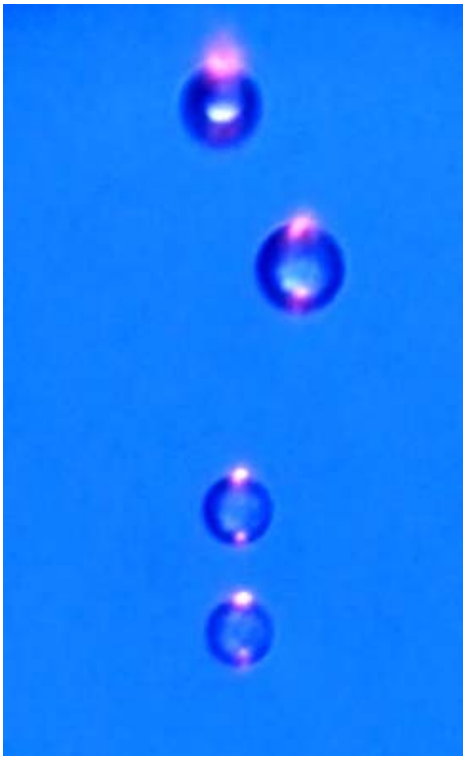

Figure 6.2: Photograph of bright red spots at the azimuth of each trapped 25μm silica sphere, corresponding to whispering gallery modes. The spheres are levitated on a high power infrared laser, and a low power red laser is used to observe so-called glare points

Trapping of $7\mu m$ silica microspheres can be accomplished at optical powers of less than 10mW. In order to investigate the interaction of trapped objects with each other, however, higher optical powers, up to 1W, were used. Spheres are dispersed randomly in the vicinity of the optical trap, and complex configurations form with objects falling into the trap one or severally at a time.

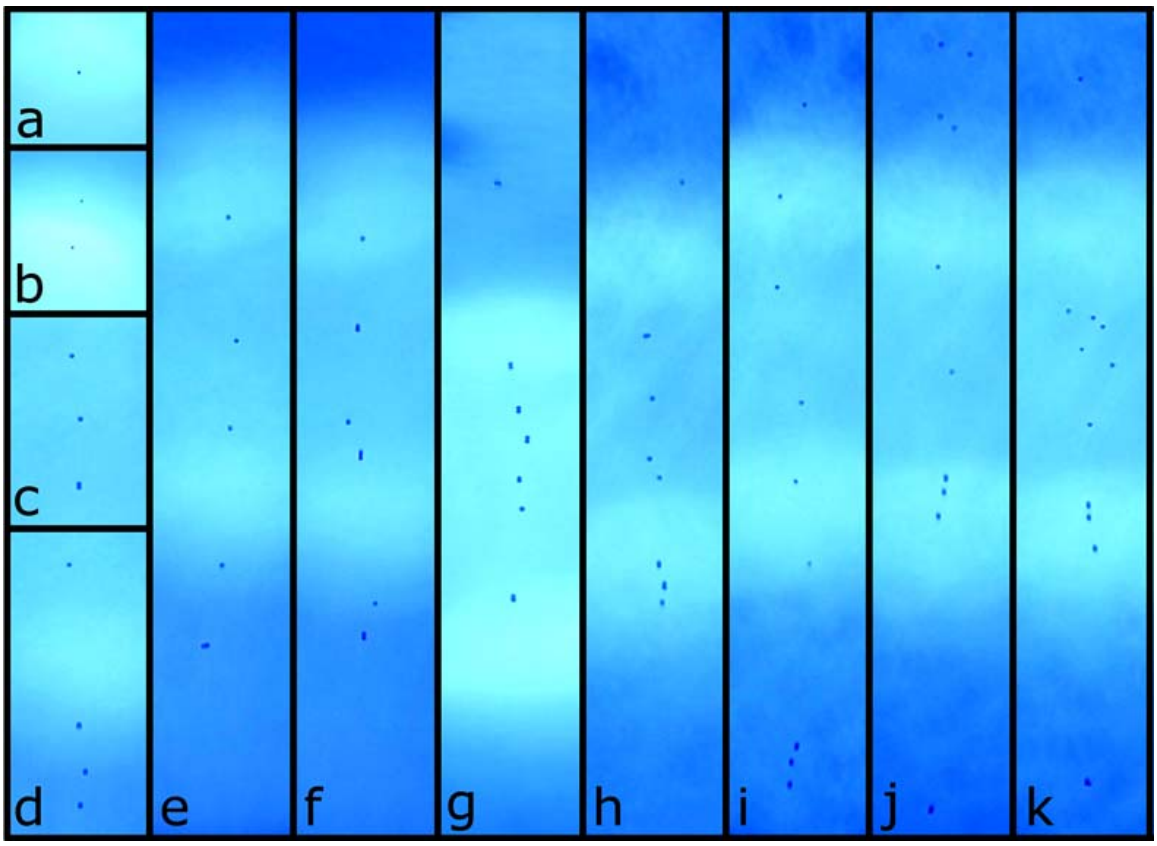

Figure 6.3: Experimental images of optical clustering cofigurations for 7μm silica spheres in air. Number of discrete trapped particles at 500mW optical power ranges from (a) one to (k) eleven

6.2.2 Harmonic Motion

Clustering of varying numbers of particles is observed in the trap at a power of 500mW, as shown in Figure 6.3. A variety of stable and dynamic configurations are observed for all size ranges. Surprisingly, clustering is versatile as it occurs also when non-spherical particles that are formed from physically attached spheres are suspended and clustered in various configurations as shown above. Trapped objects remain suspended for minutes, up to a several hours, even with large numbers or highly dynamic behavior.

The dynamic arrangements created by the interaction of trapped particles range

from simple, approximately harmonic motion, to complex and disordered behavior. Figure 6.4 shows the time evolution of two trapped 7μm spheres which oscillate in a quasi-harmonic pattern. Figure 6.4(a) shows photographs of the two objects over one half period of oscillation. Under similar experimental conditions, we have observed several instances of such periodic motion lasting from a few seconds up to several minutes. The vertical (along the laser propagation direction) separation of the two spheres is shown in Fig. 6.4(b) over a period of 4 seconds. As shown in (78), although the two objects move diffusively together in the trap due to the weak optical gradient forces, there are discrete separation distances at which the objects are more likely to be found. This is demonstrated in Fig. 6.4(c), a histogram of the object separation over a time of 100 seconds. The oscillation frequency is about 3Hz (Fig. 6.4(d)), and so the histogram represents 300 oscillation periods. The distance between the two preferred positions is 35μm, about 23 wavelengths. The quality factor $f/\delta f$ of the Fourier spectrum is approximately 70, and so the oscillations in our system are in the underdamped regime, in contrast to the interaction of trapped particles in liquid media described previously (83).

The observed harmonic motion under steady state excitation provides evidence of nonlinearity in the coupling between trapped objects (84). As observed in other systems of coupled oscillators, including lasers, circuits, and processes in living cells (85), the interaction of nonlinear oscillators can produce quasi-harmonic oscillations. Although a full investigation of this phenomenon is beyond the scope of this work, the finite element modeling described below provides evidence of the modification of the trapping potential by the trapped objects, which helps to explain this behavior.

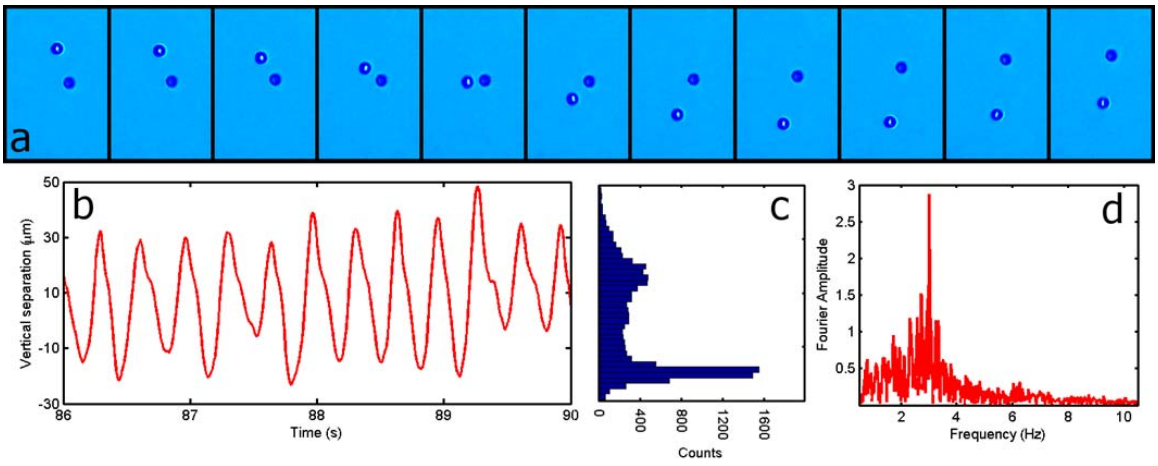

Figure 6.4: Time evolution of harmonically oscillating microspheres in an optical trap. Two 7μm silica microspheres (a) photographed over one half-period of oscillation (b) partial time domain plot of the vertical separation of the objects (c) histogram of particle positions over 100 seconds of oscillation, showing two preferred spacings, and (d) Fourier transform of vertical separation data, oscillation is approximately 3Hz

6.2.3 Disordered Motion

For larger numbers of interacting objects, the behavior transitions from periodic oscillation to disordered, random motion. Figure 6.5 shows the paths traced by five trapped objects over the course of 45 seconds. Each colored line shows the path traced by one object, up to the time indicated on the image. It can be seen that the trapped particles initially move in small areas near their original positions. However, over time the objects move far from these locations, interchanging locations many times and forming new configurations. After less than one minute, an area of 40×450μm has been covered almost completely by the trajectories of the five trapped objects.

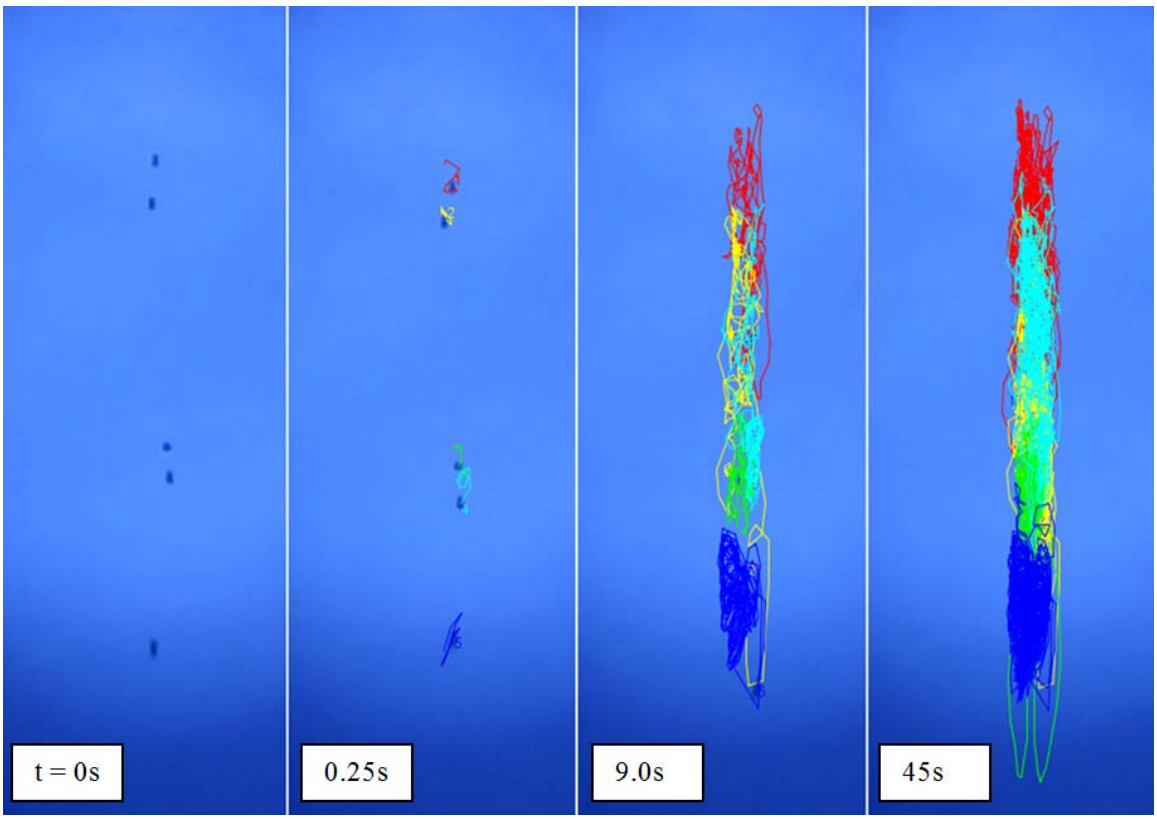

Figure 6.5: Time evolution of the trajectories of five trapped objects. The particles initially move in small, random orbits near their original positions, but over time exchange places to form new configurations, eventually covering almost completely and area of 40 450μm

6.2.4 Finite Element Modeling

The long range interaction of the trapped objects, as well as the three dimensional configurations observed, have been investigated using finite element modeling (FEM). Because the size of the trapped objects is in the Mie scattering range, between the Rayleigh scattering regime and the regime of geometric optics, analytical modeling is challenging. Lorenz-Mie theory (86; 7) offers solutions for the simple case of a dielectric sphere, but solving for more than one trapped objects is still computationally intense (87). For our case, where many of the objects of interest are formed by nonspherical clumps of microspheres, the FEM approach was deemed the best

solution.

When the trapped objects are spherical and much larger than the wavelength, each object behaves similarly to a simple ball lens with back focal length

$$f_B = \frac{nD}{4(n-1)} - \frac{D}{2} \tag{6.1}$$

where n is the refractive index and D is the sphere diameter. For 25μm silica microspheres, $f_B = 7.64\mu$m. For 7μm diameter, $f_B = 2.14\mu$m. The refocusing of light through the trapped spheres creates new trapping potentials higher up. Figure 6.6 shows an experimental photograph of 4 microspheres, nominally 25μm diameter, confined to the same optical trap at an optical power of 500mW, with a beam waist of 20μm. Figure 6.6(b) shows the intensity distribution produced by the refocusing of the light by the microspheres. Because the scattering force is expected to dominate, trapped objects can be displaced from the intensity maxima in the direction of propagation, as is the case in Fig. 6.6.

For objects closer in size to the optical wavelength trapped in a weakly focused Gaussian beam, the situation is more complicated. Light that is refocused by the trapped object interferes with light traveling around the object, creating more complex potentials above the object. This interference is sensitive to changes in the object size and position. Figure 6a shows the intensity pattern produced by the same Gaussian beam by scattering from a (a) 6, (b) 7, and (c) 8μm diameter silica microspheres.

Depending on size variations, a single trapped microsphere can refocus the beam in the propagation direction, as in Fig. 6.6. Perhaps counterintuitively, this simple situation can also produce off-axis intensity maxima, as shown in Fig. 6.7. This qualitatively explains the experimentally observed behavior of larger number of 7μm

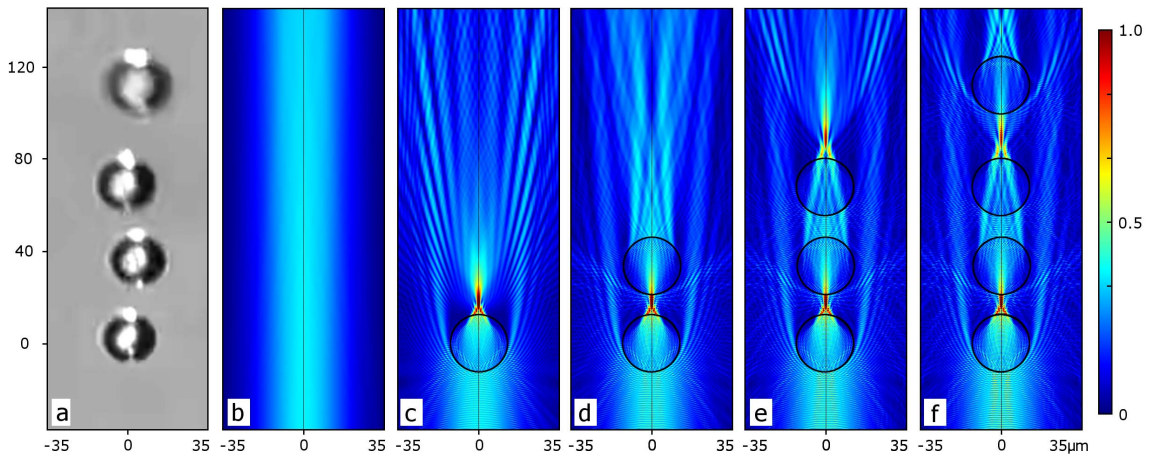

Figure 6.6: Finite element modeling of four silica microspheres, diameter 25μm, confined to a weakly focused Gaussian beam trap. Adding objects creates new intensity maxima, which act as potential wells for trapping additional objects

spheres, which are often trapped in complex 3D configurations. An example of this behavior is modeled in Fig. 6.8. The photograph in Fig. 6.8(a) shows three trapped objects, composed of either one or two 7μm silica spheres. The trapping potential created by the lowest sphere creates a new potential, which is in turn modified by the second object, composed of two spheres. The intensity profile in Fig. 6.8 illustrates how the single Gaussian potential well can be scattered to create a complex array of potential wells capable of trapping additional objects.

6.3 Conclusion

We have demonstrated the long range optical binding of silica objects in air. Optically trapped objects refocus and scatter the weakly focused Gaussian trapping beam, creating additional trapping potentials higher up. The trapped objects influence each others positions, producing simple, approximately harmonic motion in the case of two trapped microspheres, and complex disordered motion when more objects are added

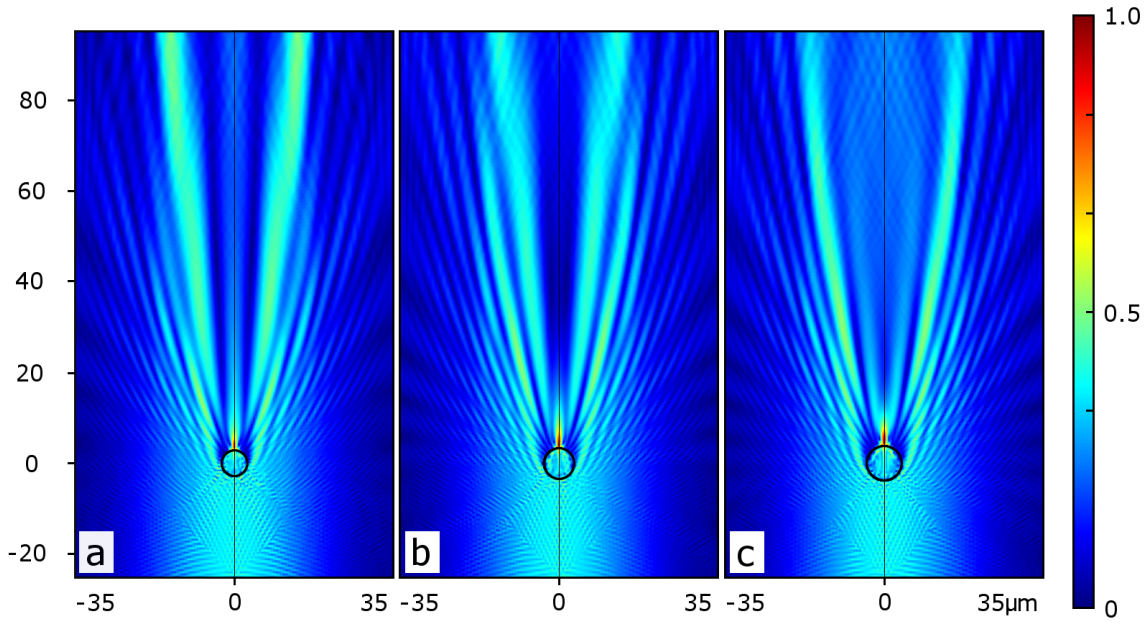

Figure 6.7: Finite element modeling of a single silica microsphere, trapped at the focus of a single Gaussian beam trap. Interference of refocused light and light traveling around the sphere results in a complex intensity profile which depends strongly on the size of the trapped object. In reality, the trapped object will be displaced beyond the beam focus, due to the high power and weak focus of the beam

to the trap.

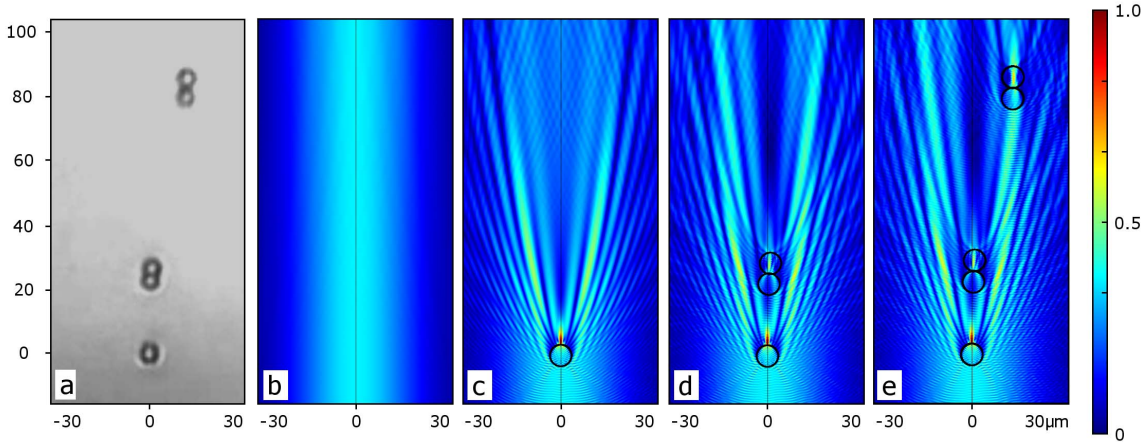

Figure 6.8: Simulation of one spherical and two nonspherical objects confined to a weakly focused Gaussian beam trap. The objects modify the trapping potential, producing additional traps above

CHAPTER VII

Conclusion

The work presented in this dissertation addresses two major topics: optical harmonic generation in a whispering gallery resonator and long-range optical binding of aerosols.

7.1 Harmonic Generation in a Lithium Niobate Whispering Gallery Resonator

The experimental demonstration of harmonic generation extending to the ultraviolet range in a lithium niobate whispering gallery resonator is a contribution to nonlinear optics. The difficulties inherent in scaling lasers to shorter wavelengths, together with the wide range of applications for coherent ultraviolet sources, has led to the development of alternative methods. Harmonic generation is a phenomenon which enables extending the emission wavelength of a pump laser to produce coherent ultraviolet light, unrestricted by the $1/\lambda^5$ energy scaling relation which complicates the development of UV lasers. To date, very short-wavelength sources have required high pump power levels that could generally be achieved only by ultra-short pump pulses (49; 50; 51; 52; 53). Resonant enhancement is an alternative to ultra-short pump pulses for providing the high field intensities required for efficient nonlinear effects.

Toward this goal, a lithium niobate whispering gallery resonator was employed to realize the generation of a continuous-wave ultraviolet emission from a telecom-compatible near infrared pump laser. The major results of this project are summarized as follows:

1. The experimental demonstration of fourth harmonic generation at ultraviolet wavelengths from an infrared source, via cascaded second order effects in the lithium niobate resonator
    (a) Direct recording of emitted harmonics, decoupled via a diamond prism, on a CCD camera
    (b) Recording of harmonic wavelengths, collected via residual Rayleigh scattering, on a series of spectrum analyzers
    (c) Demonstration of harmonic tunability by scanning the pump laser over a 10nm range
    (d) Confirmation of second, third, and fourth order dependence of harmonic power on pump power
2. Experimental observation of multiphoton Raman scattering processes in the same device
    (a) Measurement of Raman scattering from the 1550nm pump laser
    (b) Observation of additional generated wavelengths in the near infrared, visible, and ultraviolet, due to multiphoton processes involving the pump laser, generated harmonics, and Raman lines.

This work provides a demonstration of some of the possibilities in nonlinear optics provided by crystalline whispering gallery resonators, and contributes to the catalog of effects demonstrated using such resonators for intensity enhancement. It also provides a proof of concept for further wavelength conversion experiments in similar devices.

There are several challenges which must be addressed in order to extend this work into the high harmonic regime. In particular, the opacity of lithium niobate at shorter wavelengths requires a change of approach. Still, the first steps in this journey, demonstrated here, can be followed toward the extreme by adding structures such as in (68) as suggested in (69).

7.2 Long-Range Optical Binding of Aerosols

The study of light mediated interactions between objects in a single-potential well trap in air is an experimental contribution to the study of optical trapping, and more specifically optical binding. The manipulation of microscopic objects with laser light has been an area of interest since the early demonstrations in the 1970s (72). More recently, optical binding, the study of interactions between trapped objects, has become a scientific field in its own right (78; 73; 74; 79; 80).

The major results of our investigation of optical binding in air are:

1. The experimental observation of complex configurations of many objects, both spherical and aspherical, confined to a single Gaussian beam trap
    (a) Recording static and dynamic behavior of trapped objects in groups ranging from two to twenty trapped objects
    (b) Analysis of quasi-harmonic oscillation of trapped objects
    (c) Observation of more complicated interactions with larger numbers of trapped objects
2. Finite element modeling of the trapping potential created by dielectric objects in a weakly focused Gaussian beam trap
    (a) Analysis of the modified intensity profile for spherical objects which are larger (25μm) and on the order of (7μm) the optical wavelength

(b) Simulation of the complex intensity profile created by groups of nonspherical trapped objects, which can explain the complex configurations observed experimentally

This work contributes to previous experimental and theoretical study of optical binding. We provide examples of light mediated interactions between trapped objects in air at distances of many wavelengths. We also provide the beginnings of a numerical simulation framework for understanding the modification of the trapping beam by trapped objects. It is hoped that these results will be of use in the larger field of optical binding.

APPENDICES

APPENDIX A

Whispering Gallery Resonance Calculation for Dielectric Sphere

The following code calculates the resonant whispering gallery modes of a dielectric microsphere. The default values are refractive index $n = 1.46$, for fused silica, and radius $a = 100\mu m$.

```
c = 3 10^8; (*speed of light*)
mi = 146/100; (*refrativeindexmi = 1.46*)

a = 50; (*radius of spherical whispering gallery resonator in microns*)
λ0 = 155/100; (*freespacewavelength = 1.55microns*)

m = Round[2π(a)mi/λ0]

(*approximate azimuthal mode number*)
n = m;

(*Define Bessel and Hankel functions*)
```

```
J[n_, x_] = SphericalBesselJ[n, x];
H2[n_, x_] = SphericalBesselJ[n, x] - i SphericalBesselY[n, x];

ψ[n_, x_] = x J[n, x];
ψt[n_, x_] = ∂x ψ[n, x];

ξ[n_, x_] = x H2[n, x];
ξt[n_, x_] = ∂x ξ[n, x];

(*solve for dimensionless size parameter x0*)
x0 = FindRoot [Abs [ψt[n, mi x]/ψ[n, mi x] - mi ξt[n, x]/ξ[n, x]] == 0,
{x, 209}, AccuracyGoal → 50,
WorkingPrecision → 120][[1]][[2]];

(*useful parameters*)
ν0 = x0c/(2πa);
k = x0/a;
λ = 2π/k;


(*Calculate E - fieldprofile*)
β[x_]:=ψt[n, mi x]/ψ[n, mi x] - mi ξt[n, x]/ξ[n, x];
βE = J[n, mi k a]/H2[n, k a];
Fr[r_]:=J[n, mi k r] UnitStep[a - r] + β EH2[n, k r] UnitStep[r - a];

Fθ[n_, m_, θ_]:=√((2m+1)/(4π) (m-m)!/(m+m)!) n/Sin[θ] LegendreP[n, m, Cos[θ]];
```

```
(*Plot Results*)
Clear[x, y];
r = Sqrt[x^2 + y^2];
θ = π/2 - ArcTan[x, y];
DensityPlot[Re[Fr[r]]Fθ[n, n, θ], {x, .5a, 2a}, {y, -a, a},
PlotPoints → 40, ColorFunction → "Rainbow",
AspectRatio → 1, PlotRange → All]
```

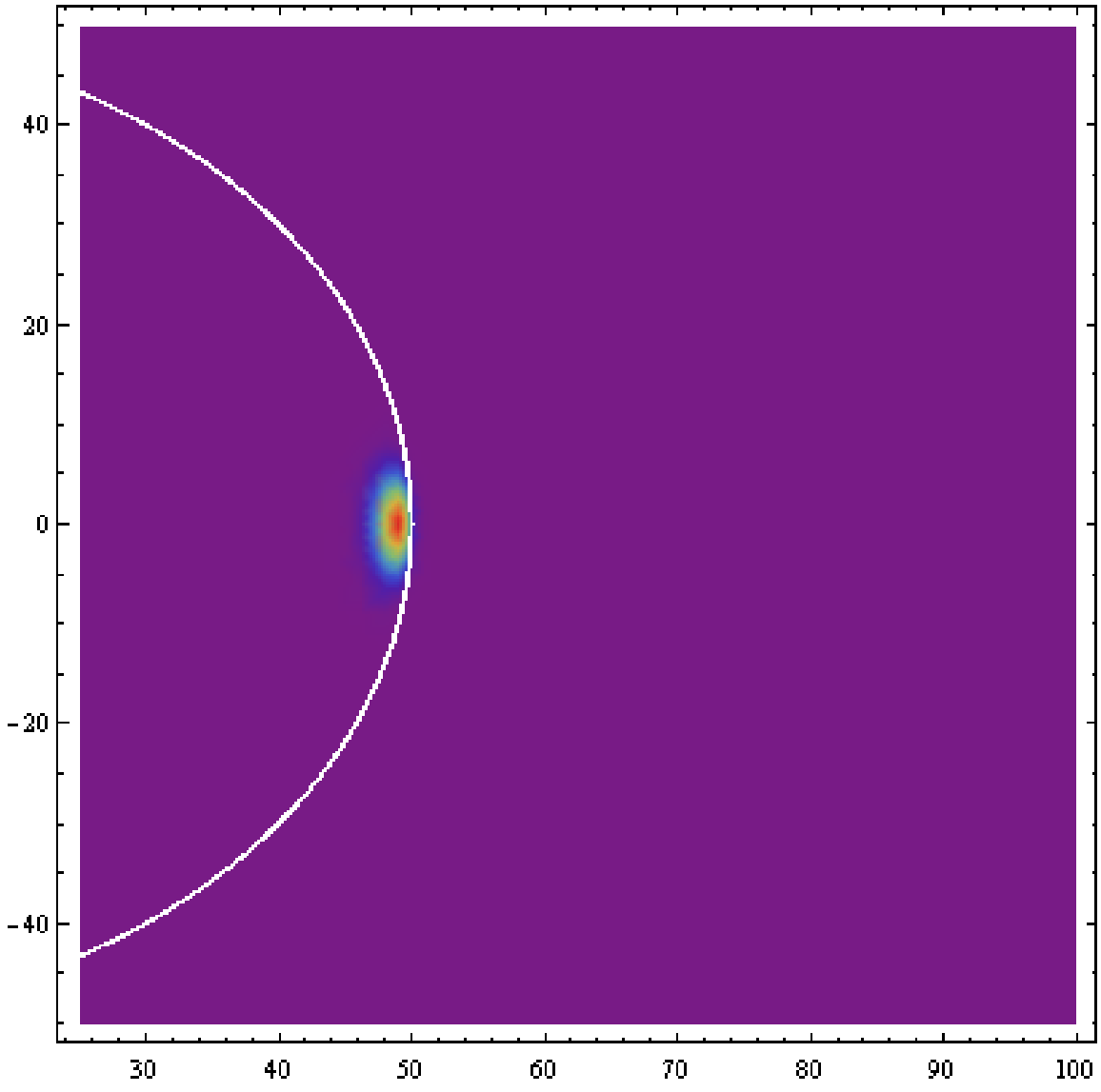

Figure A.1: Intensity profile for 100μm diameter silica microsphere near 1.55μm wavelength

APPENDIX B

COMSOL Multiphysics with MATLAB Code for Weak Gaussian Beam Trap

The following code defines a 2D numerical simulation of a dielectric object in a weakly focused Gaussian beam. The code was generated from a COMSOL Multiphysics model saved as a MATLAB file. The default geometry is a 7μm silica sphere in air, at the focus of a Gaussian beam with waist 20μm, with free space wavelength λ=1.55μm.

```
function out = model
%
% WeakGaussianOpticalTrap.m
% Model exported by COMSOL

import com.comsol.model.*
import com.comsol.model.util.*

model = ModelUtil.create('Model');
```

```
model.modelPath('C:\Users\yourname\Desktop');

model.name('1object_finemesh.mph');

model.param.set('w0', '20e-6', 'Minimum spot radius of laser');
model.param.set('lambda0', '1.55e-6',...
    'Wavelength of input laser beam');
model.param.set('c', '3e8');
model.param.set('zr', 'pi*w0^2/lambda0', 'Rayleigh range');
model.param.set('kp', '2*pi/lambda0', 'Propagation constant');
model.param.set('omega0', 'kp*3e8', 'Angular frequency');
model.param.set('P0', '0.8', 'total beam power (W)');
model.param.set('eps0', '8.854e-12',...
    'permittivity of free space');
model.param.set('E0', 'sqrt(4*P0/(eps0*c*w0*pi))');
model.param.set('spherexcenter',...
    '3.5e-6', 'Parametric sweep value');

model.modelNode.create('mod1');

model.func.create('an1', 'Analytic');
model.func.create('an2', 'Analytic');
model.func('an1').set('funcname', 'w');
model.func('an1').set('expr', 'w0*sqrt(1+(y/zr)^2)');
model.func('an1').set('args', {'y'});
model.func('an1').set('plotargs', {'y' '' ''});
model.func('an2').set('funcname', 'R');
```

```
model.func('an2').set('expr', 'y*(1+(zr/y)^2)');
model.func('an2').set('args', {'y'});
model.func('an2').set('plotargs', {'y' '' ''});

model.geom.create('geom1', 2);
model.geom('geom1').angularUnit('rad');
model.geom('geom1').feature.create('r1', 'Rectangle');
model.geom('geom1').feature.create('r2', 'Rectangle');
model.geom('geom1').feature.create('c1', 'Circle');
model.geom('geom1').feature('r1').set('pos',...
    {'-35e-6' '-25e-6'});
model.geom('geom1').feature('r1').set('size',...
    {'35e-6' '120e-6'});
model.geom('geom1').feature('r2').set('pos',...
    {'0' '-25e-6'});
model.geom('geom1').feature('r2').set('size',...
    {'35e-6' '120e-6'});
model.geom('geom1').feature('c1').set('pos',...
    {'0' '0'});
model.geom('geom1').feature('c1').set('r',...
    'spherexcenter');
model.geom('geom1').run;

model.view.create('view2', 2);

model.material.create('mat1');
model.material('mat1').propertyGroup.create...
```

```
    ('RefractiveIndex','Refractive index');
model.material.create('mat2');
model.material('mat2').propertyGroup.create...
    ('RefractiveIndex', 'Refractive index');
model.material('mat2').selection.set([3 4]);

model.physics.create('emw', 'ElectromagneticWaves', 'geom1');
model.physics('emw').feature.create('sctr1', 'Scattering', 1);
model.physics('emw').feature...
    ('sctr1').selection.set([1 2 3 4 6 7 8 9]);
model.physics('emw').feature.create...
    ('sctr2', 'Scattering', 1);
model.physics('emw').feature...
    ('sctr2').selection.set([2 5]);

model.mesh.create('mesh1', 'geom1');
model.mesh('mesh1').feature.create('ftri2', 'FreeTri');
model.mesh('mesh1').feature('ftri2').selection.geom('geom1');

model.result.table.create('evl2', 'Table');
model.result.table.create('tbl1', 'Table');

model.view('view1').axis.set('xmin', '-7.218758400995284E-5');
model.view('view1').axis.set('xmax', '7.218758400995284E-5');
model.view('view1').axis.set('ymin', '-3.3260283089475706E-5');
model.view('view1').axis.set('ymax', '1.0326028859708458E-4');
model.view('view2').axis.set('xmin', '-2.0562915779009927E-6');
```

```
model.view('view2').axis.set('xmax', '2.205629243690055E-5');
model.view('view2').axis.set('ymin', '1.9499999325489625E-5');
model.view('view2').axis.set('ymax', '3.0499999411404133E-5');
model.view('view2').axis.set('preserveaspect', false);

model.material('mat1').name('air');
model.material('mat1').propertyGroup...
    ('RefractiveIndex').set('n',...
    {'1' '0' '0' '0' '1' '0' '0' '0' '1'});
model.material('mat2').name('silica');
model.material('mat2').propertyGroup...
    ('RefractiveIndex').set('n',...
    {'1.46' '0' '0' '0' '1.46' '0' '0' '0' '1.46'});

model.physics('emw').feature('wee1').set...
    ('DisplacementFieldModel',...
    'RefractiveIndex');
model.physics('emw').feature('sctr2').set('E0i',...
    {'0'; '0'; ...
    'E0*w0/w(y[1/m])*exp(-(x[1/m])^2/w(y[1/m])^2)'...
    '*exp(-i*(kp*y[1/m]-atan(y[1/m]/zr)+'...
    'kp*(x[1/m])^2/(2*R(y[1/m]))))'});
model.physics('emw').feature('sctr2').set...
    ('kdir', {'-emw.nx'; '-emw.ny'; '0'});

model.mesh('mesh1').feature('size').set('hmax', '3E-7');
model.mesh('mesh1').feature('size').set('hmin', '2.0E-8');
```

```
model.mesh('mesh1').feature('size').set('hcurve', '0.2');
model.mesh('mesh1').feature('size').set('hgrad', '1.1');
model.mesh('mesh1').feature('size').set('hauto', '1');
model.mesh('mesh1').feature('size').set('hmax', '3E-7');
model.mesh('mesh1').feature('size').set('hmin', '2.0E-8');
model.mesh('mesh1').run;

model.result.table('evl2').name('Evaluation 2D');
model.result.table('evl2').comments('Interactive 2D values');
model.result.table('tbl1').comments...
    ('Surface Maximum 1 (emw.normE)');

model.study.create('std1');
model.study('std1').feature.create('freq', 'Frequency');

model.sol.create('sol1');
model.sol('sol1').study('std1');
model.sol('sol1').attach('std1');
model.sol.create('sol2');
model.sol('sol2').study('std1');
model.sol.create('sol3');
model.sol('sol3').study('std1');
model.sol.create('sol4');
model.sol('sol4').study('std1');
model.sol.create('sol5');
model.sol('sol5').study('std1');
model.sol.create('sol6');
```

```
model.sol('sol6').study('std1');
model.sol.create('sol7');
model.sol('sol7').study('std1');
model.sol.create('sol8');
model.sol('sol8').study('std1');
model.sol.create('sol9');
model.sol('sol9').study('std1');
model.sol.create('sol10');
model.sol('sol10').study('std1');
model.sol.create('sol11');
model.sol('sol11').study('std1');
model.sol.create('sol12');
model.sol('sol12').study('std1');
model.sol.create('sol13');
model.sol('sol13').study('std1');
model.sol.create('sol14');
model.sol('sol14').study('std1');
model.sol.create('sol15');
model.sol('sol15').study('std1');
model.sol.create('sol16');
model.sol('sol16').study('std1');
model.sol.create('sol17');
model.sol('sol17').study('std1');
model.sol.create('sol18');
model.sol('sol18').study('std1');
model.sol.create('sol19');
model.sol('sol19').study('std1');
```

```
model.sol.create('sol20');
model.sol('sol20').study('std1');
model.sol.create('sol21');
model.sol('sol21').study('std1');
model.sol('sol1').feature.create('st1', 'StudyStep');
model.sol('sol1').feature.create('v1', 'Variables');
model.sol('sol1').feature.create('s1', 'Stationary');
model.sol('sol1').feature('s1').feature.create...
    ('fc1', 'FullyCoupled');
model.sol('sol1').feature('s1').feature.remove('fcDef');
model.sol('sol2').feature.create('su1', 'StoreSolution');
model.sol('sol2').feature.create('su2', 'StoreSolution');
model.sol('sol2').feature.create('su3', 'StoreSolution');
model.sol('sol2').feature.create('su4', 'StoreSolution');
model.sol('sol2').feature.create('su5', 'StoreSolution');
model.sol('sol2').feature.create('su6', 'StoreSolution');
model.sol('sol2').feature.create('su7', 'StoreSolution');
model.sol('sol2').feature.create('su8', 'StoreSolution');
model.sol('sol2').feature.create('su9', 'StoreSolution');
model.sol('sol12').feature.create('su1', 'StoreSolution');
model.sol('sol12').feature.create('su2', 'StoreSolution');
model.sol('sol12').feature.create('su3', 'StoreSolution');
model.sol('sol12').feature.create('su4', 'StoreSolution');
model.sol('sol12').feature.create('su5', 'StoreSolution');
model.sol('sol12').feature.create('su6', 'StoreSolution');
model.sol('sol12').feature.create('su7', 'StoreSolution');
model.sol('sol12').feature.create('su8', 'StoreSolution');
```

```
model.sol('sol12').feature.create('su9', 'StoreSolution');

model.result.dataset('dset3').set('solution', 'sol12');
model.result.dataset.remove('dset4');
model.result.dataset.remove('dset5');
model.result.dataset.remove('dset6');
model.result.dataset.remove('dset7');
model.result.dataset.remove('dset8');
model.result.dataset.remove('dset9');
model.result.dataset.remove('dset10');
model.result.dataset.remove('dset11');
model.result.dataset.remove('dset12');
model.result.dataset.remove('dset13');
model.result.dataset.remove('dset14');
model.result.dataset.remove('dset15');
model.result.dataset.remove('dset16');
model.result.dataset.remove('dset17');
model.result.dataset.remove('dset18');
model.result.dataset.remove('dset19');
model.result.dataset.remove('dset20');
model.result.dataset.remove('dset21');
model.result.dataset.remove('dset22');
model.result.dataset.remove('dset23');
model.result.dataset.remove('dset24');
model.result.dataset.remove('dset25');
model.result.dataset.remove('dset26');
model.result.dataset.remove('dset27');
```

```
model.result.dataset.remove('dset28');
model.result.dataset.remove('dset29');
model.result.dataset.remove('dset30');
model.result.dataset.remove('dset31');
model.result.dataset.remove('dset32');
model.result.dataset.remove('dset33');
model.result.dataset.remove('dset34');
model.result.dataset.remove('dset35');
model.result.dataset.remove('dset36');
model.result.dataset.remove('dset37');
model.result.dataset.remove('dset38');
model.result.dataset.remove('dset39');
model.result.numerical.create('max1', 'MaxSurface');
model.result.numerical('max1').selection.all;
model.result.numerical('max1').set('probetag', 'none');
model.result.create('pg1', 'PlotGroup2D');
model.result('pg1').feature.create('surf1', 'Surface');
model.result.create('pg2', 'PlotGroup1D');
model.result('pg2').set('probetag', 'none');
model.result('pg2').feature.create('lngr1', 'LineGraph');
model.result('pg2').feature('lngr1').selection.set([4 6 7]);
model.result.create('pg3', 'PlotGroup2D');
model.result('pg3').feature.create('surf1', 'Surface');
model.result.export.create('anim1', 'Animation');

model.study('std1').feature('freq').set('plist', '1.93e14');
```

```
model.sol('sol1').feature('st1').name...
    ('Compile␣Equations:␣Frequency␣Domain');
model.sol('sol1').feature('st1').set('studystep', 'freq');
model.sol('sol1').feature('v1').set('control', 'freq');
model.sol('sol1').feature('s1').set('control', 'freq');
model.sol('sol1').feature('s1').feature...
    ('aDef').set('complexfun', true);
model.sol('sol1').runAll;
model.sol('sol2').name('Parametric␣2');
model.sol('sol2').feature('su1').name('Store␣Solution␣3');
model.sol('sol2').feature('su1').set('sol', 'sol3');
model.sol('sol2').feature('su2').name('Store␣Solution␣4');
model.sol('sol2').feature('su2').set('sol', 'sol4');
model.sol('sol2').feature('su3').name('Store␣Solution␣5');
model.sol('sol2').feature('su3').set('sol', 'sol5');
model.sol('sol2').feature('su4').name('Store␣Solution␣6');
model.sol('sol2').feature('su4').set('sol', 'sol6');
model.sol('sol2').feature('su5').name('Store␣Solution␣7');
model.sol('sol2').feature('su5').set('sol', 'sol7');
model.sol('sol2').feature('su6').name('Store␣Solution␣8');
model.sol('sol2').feature('su6').set('sol', 'sol8');
model.sol('sol2').feature('su7').name('Store␣Solution␣9');
model.sol('sol2').feature('su7').set('sol', 'sol9');
model.sol('sol2').feature('su8').name('Store␣Solution␣10');
model.sol('sol2').feature('su8').set('sol', 'sol10');
model.sol('sol2').feature('su9').name('Store␣Solution␣11');
model.sol('sol2').feature('su9').set('sol', 'sol11');
```

```
model.sol('sol3').name('Store Solution 3');
model.sol('sol4').name('Store Solution 4');
model.sol('sol5').name('Store Solution 5');
model.sol('sol6').name('Store Solution 6');
model.sol('sol7').name('Store Solution 7');
model.sol('sol8').name('Store Solution 8');
model.sol('sol9').name('Store Solution 9');
model.sol('sol10').name('Store Solution 10');
model.sol('sol11').name('Store Solution 11');
model.sol('sol12').name('Parametric 12');
model.sol('sol12').feature('su1').name('Store Solution 13');
model.sol('sol12').feature('su1').set('sol', 'sol13');
model.sol('sol12').feature('su2').name('Store Solution 14');
model.sol('sol12').feature('su2').set('sol', 'sol14');
model.sol('sol12').feature('su3').name('Store Solution 15');
model.sol('sol12').feature('su3').set('sol', 'sol15');
model.sol('sol12').feature('su4').name('Store Solution 16');
model.sol('sol12').feature('su4').set('sol', 'sol16');
model.sol('sol12').feature('su5').name('Store Solution 17');
model.sol('sol12').feature('su5').set('sol', 'sol17');
model.sol('sol12').feature('su6').name('Store Solution 18');
model.sol('sol12').feature('su6').set('sol', 'sol18');
model.sol('sol12').feature('su7').name('Store Solution 19');
model.sol('sol12').feature('su7').set('sol', 'sol19');
model.sol('sol12').feature('su8').name('Store Solution 20');
model.sol('sol12').feature('su8').set('sol', 'sol20');
model.sol('sol12').feature('su9').name('Store Solution 21');
```

```
model.sol('sol12').feature('su9').set('sol', 'sol21');
model.sol('sol13').name('Store Solution 13');
model.sol('sol14').name('Store Solution 14');
model.sol('sol15').name('Store Solution 15');
model.sol('sol16').name('Store Solution 16');
model.sol('sol17').name('Store Solution 17');
model.sol('sol18').name('Store Solution 18');
model.sol('sol19').name('Store Solution 19');
model.sol('sol20').name('Store Solution 20');
model.sol('sol21').name('Store Solution 21');

model.result.numerical('max1').set('table', 'tbl1');
model.result.numerical('max1').selection.all;
model.result.numerical('max1').setResult;
model.result('pg1').name('Electric Field (emw)');
model.result('pg1').set('data', 'dset3');
model.result('pg1').feature('surf1').set...
    ('rangecoloractive', 'on');
model.result('pg1').feature('surf1').set...
    ('rangecolormax', '12000');
model.result('pg2').set('data', 'dset3');
model.result('pg2').set('xlabel', 'y-coordinate (m)');
model.result('pg2').set('ylabel',...
    'Electric field norm (V/m)');
model.result('pg2').set('xlabelactive', false);
model.result('pg2').set('ylabelactive', false);
model.result('pg2').feature('lngr1').set('data', 'dset3');
```

```
model.result('pg2').feature('lngr1').set('xdata', 'expr');
model.result('pg2').feature('lngr1').set('xdataexpr', 'y');
model.result('pg2').feature('lngr1').set('xdataunit', 'm');
model.result('pg2').feature('lngr1').set...
    ('xdatadescr', 'y-coordinate');
model.result('pg2').feature('lngr1').set('legend', true);
model.result('pg3').name('Electric Field (emw) 1');

model.sol('sol1').clearSolution;
model.sol('sol2').clearSolution;
model.sol('sol3').clearSolution;
model.sol('sol4').clearSolution;
model.sol('sol5').clearSolution;
model.sol('sol6').clearSolution;
model.sol('sol7').clearSolution;
model.sol('sol8').clearSolution;
model.sol('sol9').clearSolution;
model.sol('sol10').clearSolution;
model.sol('sol11').clearSolution;
model.sol('sol12').clearSolution;
model.sol('sol13').clearSolution;
model.sol('sol14').clearSolution;
model.sol('sol15').clearSolution;
model.sol('sol16').clearSolution;
model.sol('sol17').clearSolution;
model.sol('sol18').clearSolution;
model.sol('sol19').clearSolution;
```

```
model.sol('sol20').clearSolution;
model.sol('sol21').clearSolution;

model.mesh.clearMeshes;

out = model;
```

BIBLIOGRAPHY

BIBLIOGRAPHY

[1] J. Moore, M. Tomes, T. Carmon, and M. Jarrahi, "Continuous-wave ultraviolet emission through fourth-harmonic generation in a whispering- gallery resonator," *Optics Express*, vol. 19, no. 24, pp. 24139–24146, 2011.

[2] J. Moore, M. Tomes, T. Carmon, and M. Jarrahi, "Continuous-wave cascaded-harmonic generation and multi-photon Raman lasing in lithium niobate whispering-gallery resonators," *Applied Physics Letters*, vol. 99, no. 22, p. 221111, 2011.

[3] J. Moore, L. Martin, K. H. Kim, H. Chandrahalim, M. Eichenfield, I. R. Martin, and T. Carmon, "Clustering of Aerosols in a Single Potential-well Trap," in *Frontiers in Optics 2013*, p. FTh1D.2, Optical Society of America, 2013.

[4] Wikimedia Commons, "St Paul's Cathedral Whispering Gallery.jpg," 2011.

[5] L. Rayleigh, "The Problem of the Whispering Gallery," *Philosophical Magazine*, vol. 20, pp. 1001–1004, 1910.

[6] P. Debye, "Der Lichtdruck auf Kugeln von beliebigem Material," *Annalen Der Physik*, vol. 335, no. 11, pp. 57–136, 1909.

[7] G. Mie, "Beitrage zur Optik truber Medien, speziell kolloidaler Metallosungen," *Annalen Der Physik*, vol. 25, no. 3, pp. 377–445, 1908.

[8] H. M. Tzeng, K. F. Wall, M. B. Long, and R. K. Chang, "Laser emission from individual droplets at wavelengths corresponding to morphology- dependent resonances," *Opt. Lett.*, vol. 9, pp. 499–501, 1984.

[9] T. Carmon and K. Vahala, "Modal Spectroscopy of Optoexcited Vibrations of a Micron-Scale On-Chip Resonator at Greater than 1 GHz Frequency," *Physical Review Letters*, vol. 98, p. 123901, Mar. 2007.

[10] M. Tomes, K. J. Vahala, and T. Carmon, "Direct imaging of tunneling from a potential well.," *Optics express*, vol. 17, pp. 19160–5, Oct. 2009.

[11] C.-y. Chao, S. Ashkenazi, S.-w. Huang, M. O. Donnell, and L. J. Guo, "High-Frequency Ultrasound Sensors Using," *IEEE Transactions on Ultrasonics, Ferroelectrics, and Frequency Control*, vol. 54, no. 5, pp. 957–965, 2007.

[12] T. Ling, S.-L. Chen, and L. J. Guo, "Fabrication and characterization of high Q polymer micro-ring resonator and its application as a sensitive ultrasonic detector.," *Optics express*, vol. 19, pp. 861–9, Jan. 2011.

[13] M. Hossein-Zadeh and K. J. Vahala, "Fiber-taper coupling to Whispering-Gallery modes of fluidic resonators embedded in a liquid medium.," *Optics express*, vol. 14, pp. 10800–10, Oct. 2006.

[14] K. Hyun Kim, G. Bahl, W. Lee, J. Liu, M. Tomes, X. Fan, and T. Carmon, "Cavity optomechanics on a microfluidic resonator with water and viscous liquids," *Light: Science & Applications*, vol. 2, p. e110, Nov. 2013.

[15] G. Bahl, X. Fan, and T. Carmon, "Acoustic whispering-gallery modes in optomechanical shells," *New Journal of Physics*, vol. 14, p. 115026, Nov. 2012.

[16] A. Savchenkov, A. Matsko, V. Ilchenko, D. Strekalov, and L. Maleki, "Direct observation of stopped light in a whispering-gallery-mode microresonator," *Physical Review A*, vol. 76, p. 023816, Aug. 2007.

[17] I. S. Grudinin, A. B. Matsko, and L. Maleki, "Brillouin Lasing with a CaF2 Whispering Gallery Mode Resonator," *Physical Review Letters*, vol. 102, p. 043902, Jan. 2009.

[18] K. Vahala, *Optical Microcavities*. World Scientific Publishing Co. Pte. Ltd., 2004.

[19] A. Matsko and V. Ilchenko, "Optical resonators with whispering-gallery modes-part I: basics," *IEEE Journal of Selected Topics in Quantum Electronics*, vol. 12, pp. 3–14, Jan. 2006.

[20] V. Ilchenko and a.B. Matsko, "Optical resonators with whispering-gallery modes-part II: applications," *IEEE Journal of Selected Topics in Quantum Electronics*, vol. 12, pp. 15–32, Jan. 2006.

[21] M. Tomes and T. Carmon, "Photonic Micro-Electromechanical Systems Vibrating at X-band (11-GHz) Rates," *Physical Review Letters*, vol. 102, p. 113601, Mar. 2009.

[22] G. Bahl, J. Zehnpfennig, M. Tomes, and T. Carmon, "Stimulated optomechanical excitation of surface acoustic waves in a microdevice.," *Nature communications*, vol. 2, p. 403, Jan. 2011.

[23] A. Savchenkov, A. Matsko, V. Ilchenko, D. Seidel, and L. Maleki, "Surface acoustic wave opto-mechanical oscillator and frequency comb generator.," *Optics letters*, vol. 36, pp. 3338–40, Sept. 2011.

[24] T. Carmon, H. Rokhsari, L. Yang, T. Kippenberg, and K. Vahala, "Temporal Behavior of Radiation-Pressure-Induced Vibrations of an Optical Microcavity Phonon Mode," *Physical Review Letters*, vol. 94, p. 223902, June 2005.

[25] T. J. Kippenberg, S. M. Spillane, and K. J. Vahala, "Kerr-nonlinearity optical parametric oscillation in an ultrahigh-Q toroid microcavity.," *Physical Review Letters*, vol. 93, no. 8, p. 083904, 2004.

[26] T. Beckmann, H. Linnenbank, H. Steigerwald, B. Sturman, D. Haertle, K. Buse, and I. Breunig, "Highly Tunable Low-Threshold Optical Parametric Oscillation in Radially Poled Whispering Gallery Resonators," *Physical Review Letters*, vol. 106, p. 143903, Apr. 2011.

[27] J. U. Fürst, D. V. Strekalov, D. Elser, a. Aiello, U. L. Andersen, C. Marquardt, and G. Leuchs, "Low-Threshold Optical Parametric Oscillations in a Whispering Gallery Mode Resonator," *Physical Review Letters*, vol. 105, p. 263904, Dec. 2010.

[28] S. M. Spillane, T. J. Kippenberg, and K. J. Vahala, "Ultralow-threshold Raman laser using a spherical dielectric microcavity," *Nature*, vol. 415, pp. 621–623, 2002.

[29] S.-X. Qian and R. K. Chang, "Multiorder Stokes Emission from Micrometer-Size Droplets," *Physical Review Letters*, vol. 56, no. 9, pp. 926–929, 1986.

[30] H.-B. Lin, A. L. Huston, J. D. Eversole, and A. J. Campillo, "Double-resonance stimulated Raman scattering in micrometer-sized droplets," *Journal of the Optical Society of America B*, vol. 7, pp. 2079–2089, Oct. 1990.

[31] L. Yang, T. Carmon, B. Min, S. M. Spillane, and K. J. Vahala, "Erbium-doped and Raman microlasers on a silicon chip fabricated by the solgel process," *Applied Physics Letters*, vol. 86, no. 9, p. 091114, 2005.

[32] V. Ilchenko, A. Savchenkov, A. Matsko, and L. Maleki, "Nonlinear Optics and Crystalline Whispering Gallery Mode Cavities," *Physical Review Letters*, vol. 92, pp. 2–5, Jan. 2004.

[33] T. Carmon and K. J. Vahala, "Visible continuous emission from a silica microphotonic device by third-harmonic generation," *Nature Physics*, vol. 3, pp. 430–435, May 2007.

[34] K. Sasagawa and M. Tsuchiya, "Highly Efficient Third Harmonic Generation in a Periodically Poled MgO:LiNbO 3 Disk Resonator," *Applied Physics Express*, vol. 2, p. 122401, Dec. 2009.

[35] D. H. Leach, R. K. Chang, W. P. Acker, and S. C. Hill, "Third-order sum-frequency generation in droplets: experimental results," *Journal of the Optical Society of America B*, vol. 10, p. 34, Jan. 1993.

[36] W. P. Acker, D. H. Leach, and R. K. Chang, "Third-order optical sum-frequency generation in micrometer-sized liquid droplets," *Optics letters*, vol. 14, pp. 402–4, Apr. 1989.

[37] J. U. Fürst, D. V. Strekalov, D. Elser, M. Lassen, U. L. Andersen, C. Marquardt, and G. Leuchs, "Naturally Phase-Matched Second-Harmonic Generation in a Whispering-Gallery-Mode Resonator," *Physical Review Letters*, vol. 104, p. 153901, Apr. 2010.

[38] M. Oxborrow, "Traceable 2-D Finite-Element Simulation of the Whispering-Gallery Modes of Axisymmetric Electromagnetic Resonators," *IEEE Transactions on Microwave Theory and Techniques*, vol. 55, pp. 1209–1218, June 2007.

[39] R. Chang and A. Campillo, "Optical resonances of a spherical dielectric microcavity: effects of perturbations," in *Optical Processes in Microcavities*, pp. 209–256, Singapore: World Scientific Publishing, 1996.

[40] T. Maiman, "Stimulated Optical Radiation in Ruby," *Nature*, vol. 187, pp. 493–494, 1960.

[41] P. Franken, A. Hill, C. Peters, and G. Weinreich, "Generation of Optical Harmonics," *Physical Review Letters*, vol. 7, no. 4, pp. 118–120, 1961.

[42] M. C. Hoffmann, K.-L. Yeh, J. Hebling, and K. a. Nelson, "Efficient terahertz generation by optical rectification at 1035 nm.," *Optics express*, vol. 15, pp. 11706–13, Sept. 2007.

[43] H. Kapteyn, O. Cohen, I. Christov, and M. Murnane, "Harnessing attosecond science in the quest for coherent X-rays.," *Science*, vol. 317, pp. 775–8, Aug. 2007.

[44] R. Boyd, *Nonlinear Optics*. Academic Press, 3rd ed., 2008.

[45] R. Terhune, P. Maker, and C. Savage, "Measurements of Nonlinear Light Scattering," *Physical Review Letters*, vol. 14, no. 17, pp. 681–684, 1965.

[46] S. J. Cyvin, J. E. Rauch, and J. C. Decius, "Theory of Hyper-Raman Effects (Nonlinear Inelastic Light Scattering): Selection Rules and Depolarization Ratios for the Second-Order Polarizability," *The Journal of Chemical Physics*, vol. 43, no. 11, p. 4083, 1965.

[47] Deltronic Crystal Industries, "crystal_boule_slt.JPG," 2012.

[48] Phonon Corporation, "MaterialsSubstrates1712.jpg," 2012.

[49] I. A. Bufetov, M. V. Grekov, K. M. Golant, E. M. Dianov, and R. R. Khrapko, "Ultraviolet-light generation in nitrogen-doped silica fiber," *Optics letters*, vol. 22, pp. 1394–6, Sept. 1997.

[50] R. A. Bartels, A. Paul, H. Green, H. C. Kapteyn, M. M. Murnane, S. Backus, I. P. Christov, Y. Liu, D. Attwood, and C. Jacobsen, "Generation of Spatially Coherent Light at Extreme Ultraviolet Wavelengths," *Science*, vol. 297, pp. 376–378, 2002.

[51] A. Paul, R. Bartels, R. Tobey, H. Green, S. Weiman, I. Christov, M. Murnane, H. Kapteyn, and S. Backus, "Quasi-phase-matched generation of coherent extreme-ultraviolet light.," *Nature*, vol. 421, pp. 51–4, Jan. 2003.

[52] T. Sekikawa, A. Kosuge, T. Kanai, and S. Watanabe, "Nonlinear optics in the extreme ultraviolet," *Nature*, vol. 432, no. December, pp. 605–608, 2004.

[53] X. Zhang, Z. Wang, G. Wang, Y. Zhu, Z. Xu, and C. Chen, "Widely tunable and high-average-power fourth-harmonic generation of a Ti:sapphire laser with a KBe2BO3F2 prism-coupled device," *Optics letters*, vol. 34, pp. 1342–4, May 2009.

[54] D. Haertle, "Domain patterns for quasi-phase matching in whispering-gallery modes," *Journal of Optics*, vol. 12, p. 035202, Mar. 2010.

[55] D. Jundt, "Properties of Lithium Niobate," in *Properties of Lithium Niobate* (K. K. Wong, ed.), ch. 8, pp. 113–140, 2002.

[56] H. A. Haus and W. Huang, "Coupled-Mode Theory," *Proceedings of the IEEE*, vol. 19, no. 10, pp. 1505–1518, 1991.

[57] P. Maker, R. Terhune, M. Nisenoff, and C. Savage, "Effects of Dispersion and Focusing on the Production of Optical Harmonics," *Physical Review Letters*, vol. 8, no. 1, pp. 21–23, 1962.

[58] V. S. Ilchenko, A. B. Matsko, A. A. Savchenkov, and L. Maleki, "Low-threshold parametric nonlinear optics with quasi-phase-matched whispering-gallery modes," *Journal of the Optical Society of America B*, vol. 20, no. 6, pp. 1304–1308, 2003.

[59] T. Carmon, H. G. L. Schwefel, L. Yang, M. Oxborrow, a. D. Stone, and K. J. Vahala, "Static Envelope Patterns in Composite Resonances Generated by Level Crossing in Optical Toroidal Microcavities," *Physical Review Letters*, vol. 100, p. 103905, Mar. 2008.

[60] M. L. Gorodetsky and V. S. Ilchenko, "Optical microsphere resonators: optimal coupling to high-Q whispering-gallery modes," *Journal of the Optical Society of America B*, vol. 16, p. 147, Jan. 1999.

[61] T. Carmon, L. Yang, and K. Vahala, "Dynamical thermal behavior and thermal self-stability of microcavities.," *Optics express*, vol. 12, pp. 4742–50, Oct. 2004.

[62] P. Bey and H. Rabin, "Coupled-Wave Solution of Harmonic Generation in an Optically Active Medium," *Physical Review*, vol. 162, no. 3, pp. 794–800, 1967.

[63] P. Bey, J. Giuliani, and H. Rabin, "Linear and Circular Polarized Laser Radiation in Optical Third Harmonic Generation," *Physics Letters*, vol. 26, no. 3, pp. 128–129, 1968.

[64] R. Schaufele and M. Weber, "Raman Scattering by Lithium Niobate," *Physical Review Letters*, vol. 152, no. 2, pp. 705–708, 1966.

[65] A. Ridah, P. Bourson, M. Fontana, and G. Malovichko, "The composition dependence of the Raman spectrum and new assignment of the phonons in LiNbO3," *Journal of Physics: Condensed Matter*, vol. 9, pp. 9687–9693, 1997.

[66] V. Denisov, B. Mavrin, V. Podobedov, and K. Sterin, "Hyper-Raman Scattering in the LiNbO3 Crystal," *Optics Communications*, vol. 26, no. 3, pp. 372–374, 1978.

[67] M. T. Simons and I. Novikova, "Observation of second-order hyper-Raman generation in LiNbO3 whispering-gallery mode disk resonators.," *Optics letters*, vol. 36, pp. 3027–9, Aug. 2011.

[68] S. Kim, J. Jin, Y.-J. Kim, I.-Y. Park, Y. Kim, and S.-W. Kim, "High-harmonic generation by resonant plasmon field enhancement.," *Nature*, vol. 453, pp. 757–60, June 2008.

[69] M. Kozlov, O. Kfir, A. Fleischer, T. Carmon, H. G. Schwefel, and O. Cohen, "High-Order Harmonics of a Continuous-Wave Driving Laser," in *Frontiers in Optics*, (Rochester, NY), p. Paper FWE2, 2010.

[70] A. Ashkin, J. Dziedzic, and T. Yamane, "Optical trapping and manipulation of single cells using infrared laser beams," *Nature*, vol. 330, no. 24, pp. 769–771, 1987.

[71] G. Bahl, M. Tomes, F. Marquardt, and T. Carmon, "Observation of spontaneous Brillouin cooling," *Nature Physics*, vol. 8, no. 3, pp. 203–207, 2012.

[72] A. Ashkin, "Acceleration and Trapping of Particles by Radiation Pressure," *Physical Review Letters*, vol. 24, no. 4, pp. 156–159, 1970.

[73] M. J. Lang and S. M. Block, "Resource Letter: LBOT-1: Laser-based optical tweezers.," *American journal of physics*, vol. 71, pp. 201–215, Mar. 2003.

[74] S. Chu, "Laser Manipulation of Atoms and Particles," *Science*, vol. 253, no. 5022, pp. 861–866, 1991.

[75] E. R. Dufresne and D. G. Grier, "Optical tweezer arrays and optical substrates created with diffractive optics," *Review of Scientific Instruments*, vol. 69, no. 5, p. 1974, 1998.

[76] M. Reicherter, T. Haist, E. U. Wagemann, and H. J. Tiziani, "Optical particle trapping with computer-generated holograms written on a liquid-crystal display.," *Optics letters*, vol. 24, pp. 608–10, May 1999.

[77] K. Visscher, G. Brakenhoff, and J. Krol, "Micromanipulation by multiple optical traps created by a single fast scanning trap integrated with the bilateral confocal scanning laser microscope," *Cytometry*, vol. 14, pp. 105–114, 1993.

[78] M. M. Burns, J.-M. Fournier, and J. A. Golovchenko, "Optical Binding," *Physical Review Letters*, vol. 63, no. 12, pp. 1233–1236, 1989.

[79] K. Dholakia and P. Zemánek, "Colloquium: Gripped by light: Optical binding," *Reviews of Modern Physics*, vol. 82, pp. 1767–1791, June 2010.

[80] J. Taylor, *Optical Binding Phenomena: Observations and Mechanisms*. Springer-Verlag Berlin Heidelberg, 2011.

[81] M. Guillon and B. Stout, "Optical trapping and binding in air: Imaging and spectroscopic analysis," *Physical Review A*, vol. 77, p. 023806, Feb. 2008.

[82] D. Rudd, C. López-Mariscal, M. Summers, a. Shahvisi, J. C. Gutiérrez-Vega, and D. McGloin, "Fiber based optical trapping of aerosols.," *Optics express*, vol. 16, pp. 14550–60, Sept. 2008.

[83] Y. Roichman, D. Grier, and G. Zaslavsky, "Anomalous collective dynamics in optically driven colloidal rings," *Physical Review E*, vol. 75, p. 020401, Feb. 2007.

[84] A. H. Nayfeh and D. T. Mook, *Nonlinear oscillations*. Wiley.com, 2008.

[85] S. Strogatz, *Sync: The Emerging Science of Spontaneous Order*. New York: Hyperion Books, 2003.

[86] L. Lorenz, "Lysbevægelsen i og uden for en af plane Lysbølger belyst Kugle," *Videnskabernes Selskabs Skrifter*, vol. 6, pp. 2–62, 1890.

[87] T. A. Nieminen, V. L. Y. Loke, A. B. Stilgoe, G. Kn, N. R. Heckenberg, H. Rubinsztein-dunlop, and A. M. Bra, "Optical tweezers computational toolbox," *Journal of Optics A*, vol. 9, 2007.